Fall 2022

Impacts of Preferential Vaporization of Multi-Component Liquid Fuels on Near-Limit Combustion Behaviors

Seungjae Lim

IMPACTS OF PREFERENTIAL VAPORIZATION OF MULTI-COMPONENT LIQUID FUELS ON NEAR-LIMIT COMBUSTION BEHAVIORS

by

Seungjae Lim

Bachelor of Science
Pukyong National University, 2014

Master of Science
Pukyong National University, 2016

Submitted in Partial Fulfillment of the Requirements

For the Degree of Doctor of Philosophy in

Mechanical Engineering

College of Engineering and Computing

University of South Carolina

2022

Accepted by:

Sang Hee Won, Major Professor

Tanvir Farouk, Committee Member

Jamil Khan, Committee Member

Shamia Hoque, Committee Member

Cheryl L. Addy, Interim Vice Provost and Dean of the Graduate School

DEDICATION

I dedicate this dissertation to everyone who had worked together with me and inspired me. My adviser, Dr. Sang Hee Won, always encouraged me to complete my work and broadened my insight about combustion through his experience and knowledge. Dr. Tanvir Farouk expanded my capability when it comes to numerical simulation that I was interested in. Stuart Nates and Dalton Carpenter shared their research progress with me. Ayuob Alwahaibi helped me a lot whenever I got in trouble. Malik Tahiyat, Sudipta Saha, Ejaz Ahmed and Ebrahim Khalil Bhuiyan made me experienced in many other research areas.

ACKNOWLEDGEMENTS

First, I would like to thank my advisor, Dr. Sang Hee Won, for his continuous support throughout the entire period of my Ph.D. degree. Also, I appreciate everyone in Combustion Lab. I would like to thank to my family for their support without any reason. Finally, I really appreciate Eunsol for unlimited support so that I can overcome any problem I had. Again, I thank everyone mentioned above, and I won't forget everyone.

ABSTRACT

Combustion technologies used in energy conversion devices involve multi-phase and multi-component combustion behaviors associated with chemical kinetic characteristics coupled with spray dynamics. For reliable engine operation, the engine operation envelope is necessarily required to be determined by near-limit combustion behaviors such as flame flashback, lean blowout, ignition, and extinction, which are influenced by both fuel chemical and physical properties. Liquid fuels are composed of a wide range of molecular structures and weights, therefore exhibiting relatively large distillation temperature range. When fuel chemical properties change during fuel vaporization, preferential vaporization effects could play a considerable role in near-limit combustion behaviors. In this regard, the objective of this study is to evaluate the role of preferential vaporization on near-limit combustion behaviors.

At first, the time scale analysis of fuel droplets for gasoline, Jet fuel, and diesel is discussed to highlight the potential importance of preferential vaporization. The potential of preferential vaporization of liquid fuels is evaluated to verify the change of global reactivity over distillation cuts. Derived Cetane Number (DCN) is introduced to represent the chemical reactivity potential of distilled fuels. The variation of DCN over the distillation cuts is discussed to elucidate the preferential vaporization impact on combustion behaviors.

The impact of preferential vaporization on flame flashback is investigated by utilizing a spray burner that can control the extent of fuel evaporation. By formulating two binary mixtures to exhibit common combustion behaviors at the fully vaporized condition, but have considerably different vaporization characteristics, flame flashback behaviors are observed at fully and partially vaporized conditions with high-speed imaging and Planar Laser Induced Fluorescence (PLIF) technique. Using Phase Doppler Particle Analyzer (PDPA), the extent of fuel vaporization and flow fluctuation are evaluated to analyze the flame flashback behavior. The relative contribution of preferential vaporization on the flashback flow velocity is evaluated through feature sensitivity analysis.

The impact of preferential vaporization on diffusion flame extinction is investigated by utilizing a counterflow burner combined with the spray burner to control the extent of fuel evaporation. The behavior of diffusion flame extinction is observed at fully and partially vaporized conditions. Binary mixtures are formulated to exhibit identical extinction behavior but have different vaporization characteristic. Transport weighted enthalpy (TWE) and radical index (Ri) are applied to analyze the behavior of flame extinction. Flow stretch induced by flow fluctuation is evaluated through PDPA measurement. The relative contribution of preferential vaporization on the diffusion flame extinction is evaluated through feature sensitivity analysis.

The interaction of isolated single droplet with premixed/diffusion flames at near extinction conditions is discussed by utilizing a counterflow burner integrated with a piezo-electric assisted single droplet generator. The extinction strain rate of premixed/diffusion flames is measured at different droplet sizes with methane and air.

Single and multi-component fuels are used to observe the impact of preferential vaporization near extinction condition. The extinction behaviors are analyzed based on TWE, Ri, and vapor pressure of liquid fuel droplets.

TABLE OF CONTENTS

LIST OF TABLES

LIST OF FIGURES

LIST OF SYMBOLS

α	Thermal diffusivity
δ_{OH}	OH thickness
θ	Half angle between two laser beams of PDPA
κ	Local flame stretch
λ	The laser wavelength of PDPA
ρ_F	Density at fuel side
ρ_O	Density at oxidizer side
τ_{flame}	The time scale of flame chemistry
$\tau_{ignition}$	The time scale of ignition chemistry
τ_{res}	Flow residence time
$\tau_{vaporization}$	The time scale of fuel vaporization (τ_{evap})
φ	Equivalence ratio
φ_g	Global equivalence ratio
$\varphi_{effective}$	Local effective equivalence ratio
A_{nozzle}	The area of burner exit
A_{PDPA}	The cross-section area of the sampling volume of PDPA
D	Droplet diameter (d)
D_a	Damkhöler number
$D_{e^{-2}}$	Laser beam diameter of PDPA

F_v	The volume fraction of vaporized fuel
K	Evaporation constant
L	Markstein length (Chapter 3) or Separation distance (Chapter 4)
Le	Lewis number
MW_{Fuel}	The molecular weight of fuel
MW_{N_2}	The molecular weight of nitrogen
P_{vap}	Vapor pressure
Q	The flow rate of liquid fuel
Q_{Fuel}	The total flow rate of liquid fuel
Ri	Radical index
$S_{L,local}$	Laminar flame speed
$S_{L,NPV}$	Laminar flame speed without preferential vaporization
$S_{overall}$	Overall burning rate
Stk	Stokes number
T_b	Distillation temperature or Boiling temperature
TWE	Transport weighted enthalpy
U_0	Mean jet velocity
U_{FB}	U_0 at flame flashback
V_F	Flow velocity at fuel side
V_O	Flow velocity at oxidizer side
X_{CH4}	Methane mole fraction
X_{Fuel}	fuel mole fraction
X_g	Global fuel mole fraction

a	Global strain rate
a_{ext}	Extinction strain rate
$a_{ext,P}$	Predicted extinction strain rate
d_{10}	Arithmetic mean diameter
d_{20}	Surface mean diameter
d_{30}	Volume mean diameter
$d_{30,initial}$	Initial d_{30} value
d_{32}	Sauter mean diameter
f	The focal length of lens of PDPA
f_{PDPA}	Sampling frequency of PDPA measurement
l_f	Flame thickness
u'	Local velocity fluctuation
ΔH_C	Heat of combustion
$[Fuel]$	Fuel concentration
$[OH]_{max}$	Peak OH concentration

LIST OF ABBREVIATIONS

CI.....Compression ignition

CPTs.....Combustion property targets

DCN ..... Derived Cetane Number

IQT.....Ignition quality tester

LBO.....Lean Blowout

MW ..... Molecular weight

NMR ..... Nuclear Magnetic Resonance

PDPA ..... Phase doppler particle analyzer

PLIF .....Planar laser-induced fluorescence

SI.....Spark ignition

TSI.....Threshold sooting index

iC8..... iso-octane

iC16..... iso-cetane

nC7.....n-heptane

nC8.....n-octane

nC10 ..... n-decane

nC12 ..... n-dodecane

nC16 ..... n-hexadecane

135 TMB ..... 1,3,5 trimethylbenzene

CHAPTER 1

INTRODUCTION

1.1 Research background

Since the Industrial Revolution, heat engines have been utilized to generate useful energy for many purposes. In 18th and 19th centuries, simple steam engines were developed to directly transfer the heat energy to kinetic energy. With the advance of engine system, the Industrial Revolution led to transition from hand production methods to mechanics including chemical reaction. Consequently, the invention of mechanized system utilizing the engines have increased the productivity of all the goods produced in factories and ultimately improved the quality of life.

As it had been found that the electric power can be converted from mechanical power and vice versa, modern power plant systems have been designed and established to transfer the energy to where we need energy through power cables. Depending on the source of heat to rotate turbine blades, the power plants are categorized by the energy sources such as coal, diesel, gas, geothermal energy, nuclear reaction, and so on. Among them, liquid fuels such as diesel and gasoline are widely used in many applications (e.g., car, aviation, and turbine engines).

The combustion technologies using liquid fuels intrinsically involve complicated multi-phase and multi-component combustion behaviors associated with complex

chemical kinetic characteristics coupled with spray injection, atomization, vaporization, turbulent mixing, and heat transfer phenomena [1-8]. Especially, in practical gas turbine engines, the combustion technologies have been developed with the understanding of combustion behaviors such as ignition, extinction, burning rate, and so on. Such a complex nature of combustion with liquid fuel spray makes it difficult to understand what is happening in the combustor of gas turbine system.

Even, modern gas turbine technology requires to have fuel flexibility to cope with difficulties from environmental issues and limited fuel supplements. By achieving the fuel flexibility, many different fuels can be selected to optimize the performance of gas turbine engines. Not only that, but it can also be helpful to resolve the emission problems associated with CO_2 and NOx by mixing many different components with the fuels used in industry. However, considering that every single component in the liquid fuels can have different physical and chemical properties, there will be considerable differences in physical and chemical properties between the components in the liquid fuels with broader fuel flexibility.

Regarding gas turbine combustion, a series of extensive experimental campaigns (e.g., [9, 10]) performed decades ago testing with only petroleum-derived fuels suggested the relative significance of fuel physical properties over chemical properties due to their direct relationships with spray dynamics. Consequently, the current ASTM standard for jet fuel specification [11] rigorously evaluates fuel physical properties (e.g., distillation temperatures, viscosity, density), whereas only a few properties (e.g., net heat of combustion, smoke point) are considered to describe fuel chemical properties. Compared to petroleum-derived jet fuels that have relatively small variations in chemical properties,

recently emerging alternative jet fuels exhibit considerable variations in their chemical properties, depending on their feedstocks and synthesis approaches [12]. Recent experimental studies [12-17] suggest that fuel chemical properties cannot be overlooked for lean blowout (LBO) conditions.

Since the historical approach based on the ASTM standard has separately evaluated the fuel physical and chemical properties and has assumed that the fuel chemical properties are given as fuel properties at fully vaporized condition, it has overlooked the change of gas phase fuel composition during the fuel evaporation process. Considering that the real fuels consist of a variety of components from many different chemical classes [1], the change in gas composition over the fuel evaporation (Preferential vaporization) will influence the combustion characteristics while injected liquid fuel is vaporizing. Recently, the potential impacts of preferential vaporization typical of multi-component real jet fuels have recently garnered an interest to understand the complex multi-phase and multi-component combustion behaviors.

Among the combustion behaviors, near-limit combustion behaviors such as LBO, flame flashback, ignition, and extinction are very important to determine the operation envelope of gas turbine engines for safe and consistent engine operation. It is known that the near-limit combustion behaviors are sensitive to the chemical kinetic characteristics of fuels. Therefore, the preferential vaporization will influence the near-limit combustion behaviors.

Figure 1.1(a) shows the changes of ignition propensity measured by the derived cetane number (DCN) for the five distillation cuts of three petroleum-derived jet fuels, prepared by an ASTM D86 distillation device. Although DCN is the applied measure by

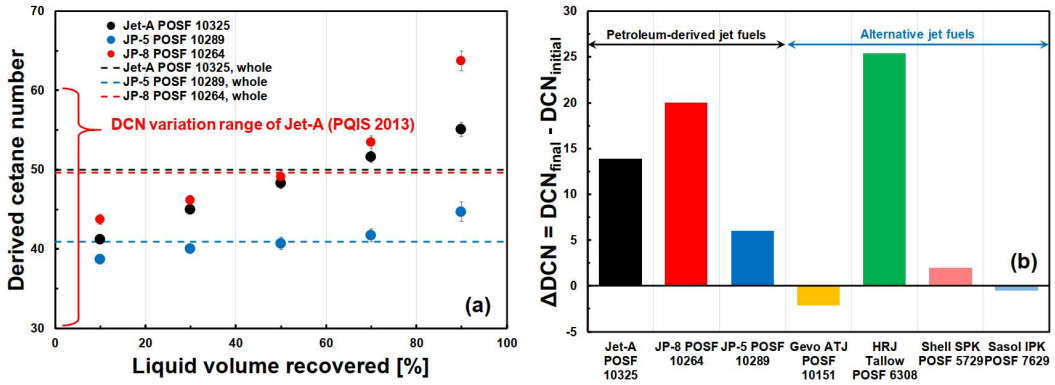

Figure 1.1. (a) The measured DCN values (chemical kinetic potential) for five distillation cuts (20 % liquid volume fraction each) of three petroleum-derived jet fuels (b) comparison of the measured DCN changes between initial and final distillation cuts, indicative of preferential vaporization potentials of petroleum-derived and alternative jet fuels.

ASTM D6890 standard, we have addressed that DCN reflects the global chemical kinetic potential of the fuel in a relative manner [18]. It is found that DCN of each distillation cut substantially changes as a function of distilled volume fraction, meaning that the chemical reactivity potential over the fuel evaporation varies depending on how much the liquid fuels are vaporized. Figure 1.1(b) summarizes the difference in DCN between the first and last distillation cuts for some petroleum-derived and alternative jet fuels. In case of HRJ Tallow, the difference is approximately 25, which means huge change of chemical reactivity potential between the initial and final cuts. Not only that, JP-8 and JP-A show quite big differences. Considering that the advanced combustion technologies optimize the engine operation with very accurate timing of ignition and/or flame stabilization, these drastic changes of chemical reactivity potential with fuel boiling characteristics can be expected to be significant.

Although the variation of chemical reactivity potential over distilled volume fraction is significant as shown in Fig. 1.1, the current applied and fundamental

approaches to consider the complicated fuel chemical and physical property impacts as previously mentioned stem from the empirical understanding established through experimentations rather than the fundamental rationale. For example, regarding aviation gas turbine combustors, Lefebvre concluded that fuel physical properties were relatively more significant, based on extensive experimental tests using three petroleum-derived liquid fuels [10]. The underlying rationale for this conclusion was that fuel physical properties govern atomization quality and vaporization rates, whereas fuel chemical properties play only a minor role through slight variations in fuel heating values. Based on this conclusion, the current spray sub-model only considers the local deposition of vapor phase fuel during the evaporation process [19], assuming no changes in fuel chemical properties during the evaporation process.

However, recent experimental observations of the near-limit combustion behavior, LBO with both petroleum-derived and alternative jet fuels suggest that under a range of conditions fuel chemical properties coupled with fuel physical properties (e.g., distillation curve) could be significant [12, 13, 20, 21]. Furthermore, in previous study, two surrogate fuels were designed to share identical combustion characteristics for fully vaporized fuel/air mixtures to those of one petroleum-derived jet fuel but have very different preferential vaporization potential [13]. The observed LBO behaviors at a rig-scale model combustor in the study suggest that the impact of preferential vaporization on LBO behaviors can be substantial even at the moderately pressurized condition (3.4 atm pressure) for the different extent of fuel vaporization by controlling the initial inlet air temperature. Although this study suggests that the potential impact of preferential vaporization on LBO behavior is considerable, it could not explain the contribution of

preferential vaporization impact on LBO due to the imposed complexity of the experimental system. In this regard, the objective of this study is to investigate the impact of preferential vaporization and to understand the fundamental physics of the preferential vaporization on near-limit combustion behaviors.

1.2 Time scale analysis on droplet combustion

Before we investigate the impact of preferential vaporization on near-limit combustion behaviors, time scale analysis has been done to identify what physics will be governing the near-limit combustion characteristics. As liquid fuel evaporation, flame chemistry, and ignition chemistry are able to be considered as main physics due to their identical characteristics, their relative impacts in multi-phase combustion with liquid fuels as a function of pressure can be evaluated by comparing their characteristics time scales. The characteristic time scale of flame chemistry (τ_{flame}) can be determined by the flame theory considering laminar flame speed, thermal diffusivity, and flame thickness. The characteristic time scale of ignition chemistry ($\tau_{ignition}$) is directly acquired by calculating the ignition delay times at given initial temperature (800 K) and pressure conditions with a detailed chemical kinetic model [22, 23]. The characteristic time scale of fuel vaporization ($\tau_{vaporization}$) is theoretically given by the initial droplet size and droplet evaporation rate following the D^2 law. In this time scale analysis, to simply this analysis, n-heptane, n-dodecane, and n-hexadecane were used as liquid fuels representing gasoline, Jet-fuel, and diesel, respectively. Initial droplet diameter is 10 μm considering the initial droplet diameter of < 50 μm typical of most fuel atomization methods [24]. The ambient temperature of 800 K is used, as typical for air inlet temperature of a gas turbine,

as well as for gas temperature after the compression stroke in both spark ignition (SI) and compression ignition (CI) engines.

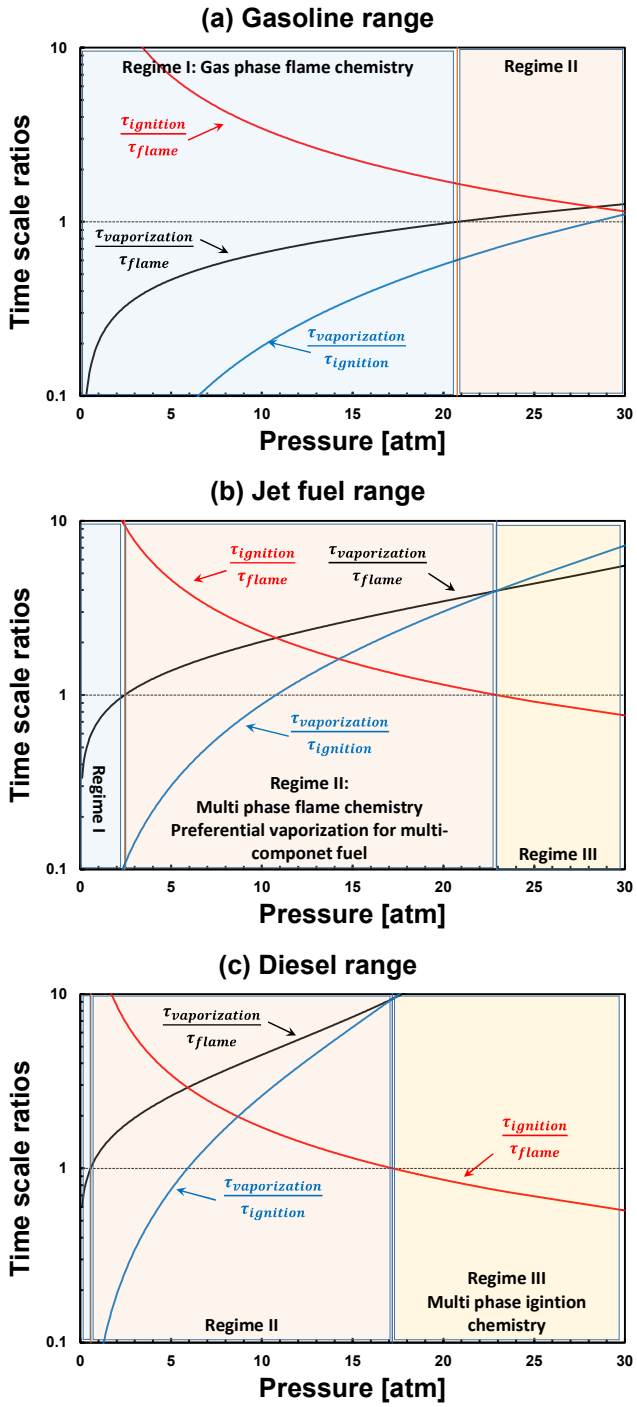

Figure 1.2. Regime diagrams based on the comparisons of characteristic time scales of fuel vaporization, flame chemistry, and ignition chemistry. (a) Jet fuel range; (b) Gasoline range; (c) Diesel range.

Figure 2 shows the three different ratios of time scales, suggesting three distinct multi-phase combustion regimes as a function of pressure based on the three different fuels. The ratios of time scales in Fig. 1.2(a) exhibit three different combustion regimes for Jet-fuels. Regime I represents gas phase flame chemistry that the time scale of fuel evaporation is the shortest compared to other time scales, meaning that liquid fuels are completely vaporized before the liquid fuel droplets reaches to the flame or ignition happens. Therefore, the gas phase flame chemistry controls the overall combustion behaviors. When $\tau_{vaporization} < \tau_{flame}$ in Regime II, the liquid fuel droplets are not fully vaporized prior to the flame reaction zone, therefore, the overall combustion behaviors will be dictated by the characteristics of fuel vaporization process coupled with flame chemistry, as multiphase flame chemistry regime. As mentioned above, the evaporation of components in multi-component fuels is governed by their physical properties (e.g., vapor pressure). Considering that the chemical properties of each component can drastically change during the fuel evaporation, it is expected that the preferential vaporization would play significant roles in flame dynamics in Regime II. Note that the transition from Regime I to Regime II occurs at ~ 2.5 atm and Regime II persists until ~ 23 atm pressure condition. At higher pressure beyond Regime II, another regime transition can be expected by comparing flame chemistry and ignition chemistry time scales. When $\tau_{ignition} < \tau_{flame}$, where the ignition chemistry will start competing against flame chemistry, the partially vaporized fuel/air mixture might exhibit auto-ignition behaviors prior to reaching the flame reaction zone. Regime III can be defined as a multiphase ignition chemistry regime.

As shown in the Fig. 1.2(a), the transitions from one regime to another are significantly affected by the vaporization characteristics of liquid fuels. Figure 1.2(b) and (c) show the rimes for gasoline and diesel fuel ranges, respectively. Since the gasoline fuels comprise relatively lighter components than Jet-fuels and diesel fuels, the regime transition from Regime I to II appears at higher pressure condition (~21 atm) due to rapid fuel vaporization, confirming that the overall combustion behaviors in SI engines are controlled by the gas-phase flame chemistry. In the case of diesel range fuels composed of relatively heavy molecules, the result shown in Fig. 1.2(c) suggests that both Regimes II and III are relevant to the CI engine.

The time scale analysis shown in Fig. 1.2 suggests that the regime diagram and transitions are highly sensitive to both fuel chemical and physical properties at the given initial droplet diameter in the spray of liquid fuels. Particularly in Regimes II and III, it is expected that the fuel droplets formed might not be fully vaporized, resulting in the presence of droplets within the flame region. Moreover, the vaporization characteristics caused by the variation of volatility of components in the liquid fuels result in the preferential vaporization. As a result, the local vaporized fractions do not align with the initial liquid phase fractions, and heavier components disproportionately remain in the liquid phase. Here, the characteristics of the ignition time scale are evaluated by the ignition delay times of the stoichiometric fuel/air mixture using a detailed chemical kinetic model. Considering the substantial change of local equivalence ratio during spray injection, atomization, and turbulent mixing, it is expected that the regime diagram is highly sensitive to the extent of fuel vaporization and to the chemical kinetic potential of vaporized fuel components. Then, the relevant question associated with the preferential

vaporization is how vaporizing components affect locally flammable conditions and their chemical reactivity potential at near-limit conditions, compared to those of original fuels.

Even though the time scale analysis has been conceptually done on multi-phase combustion behaviors, a fundamental understanding of preferential vaporization supported by experimental evidence for multi-component fuels remains a challenge, while numerical investigations using relatively simplified configuration have indicated the importance of preferential vaporization [25].

CHAPTER 2

EVALUATION OF PREFERENTIAL VAPORIZATION OF REAL FUELS

As mentioned in previous chapter, real fuels (e.g., gasoline, Jet-fuels, diesel) consist of a variety of chemical components in many different chemical classes. This fact makes it difficult to understand and evaluate combustion characteristics of the real fuels. Even, in terms of the fuel flexibility, the evaluation of combustion characteristics for real fuels and/or surrogate fuels, which are mixture to emulate target fuels with a limited number of components, needs to be carefully carried out for safe and stable operation of turbine engine system. For the formulation of surrogate fuels, the essential physical and chemical properties of surrogate fuels should be matched with those of the target fuels.

Extensive studies have attempted to produce surrogate fuels to emulate the chemical kinetic characteristic and physical properties of real target fuels. These efforts to formulate and test surrogate fuel for jet aviation fuels is well summarized [26]. It has been highlighted that physical and chemical properties as well as chemical kinetics are important and should be considered to formulate surrogate fuels. Furthermore, the global combustion characteristics of fully vaporized fuels was simplified to emulate surrogate fuels by introducing a set of reference indicators, so called “Combustion Property Targets (CPTs)” [18, 27-31].

Four CPTs have been utilized as primary consideration to identify the overall combustion characteristics and formulate surrogate fuels: hydrogen to carbon ratio (H/C ratio), derived cetane number (DCN), average molecular weight (MW), and threshold sooting index (TSI). These are selected based on the empirical understanding of how combustion behaviors might relate to each CPTs and their fundamental rationales. These CPTs are selected due to their relation to the characteristics of real fuels: autoignition, heat release rate, laminar burning rate, adiabatic flame temperature, local mixing-limited stoichiometric constant, extinction, lean blowout (LBO) limit, and sooting [30]. Therefore, the formulation of surrogate fuels can be accomplished by determining the CPTs through simple small scale experimental results.

The combustion kinetic phenomena are principally governed by the molecular structures of fuel molecules. The molecular structures influence the population of radical pool and the main heat release from the combustion process. At high temperature conditions, the reactions of $CO+OH=CO_2+H$ and $H+O_2=O+OH$ are primary to release heat and populate active radical pool, respectively. On the other hand, at low temperature conditions, the fuel oxidation process is controlled by alkyl peroxy radical isomerization process and subsequent chain branching reactions to generate peroxide intermediate species [32]. As a result, the process of population of active radical pool in a reacting system determines the overall combustion kinetic characteristics and combustion behaviors.

Among the CPTs, DCN value represents the ignition propensity of fuels evaluated by measuring the ignition delay time. The identical DCN values from different fuels implies that the overall combustion behaviors of the fuels will exhibit similar tendency as

the ignition process is highly sensitive to the process of population of active radical pool. The measurement of DCN value is carried out utilizing Ignition Quality Tester (IQT) in a specific temperature and pressure condition. As the ignition behavior is governed by the chemical kinetic characteristic of fuels, the DCN value reasonably represents the chemical reactivity potential of fuels. With the DCN value, it has found that the DCN is useful for experimentally characterizing the relative autoignition reactivity of mixtures with n-heptane and diesel fuels [32-35].

While liquid fuels are vaporizing after the injection of fuels, the chemical properties of prevaporized components will change over the fuel evaporation process. The characteristic of fuel vaporization is governed by vapor pressure. In this chapter, the preferential vaporization potential will be discussed with whole crude oils and two representative fuels, which are distilled at different temperature ranges (e.g., gasoline and Jet-fuels).

2.1 Experimental method

2.1.1 Ignition Quality Tester (IQT)

To evaluate the preferential vaporization potential of liquid fuels, DCN value is used as the indicator of the chemical reactivity potential in this study. IQT is utilized to

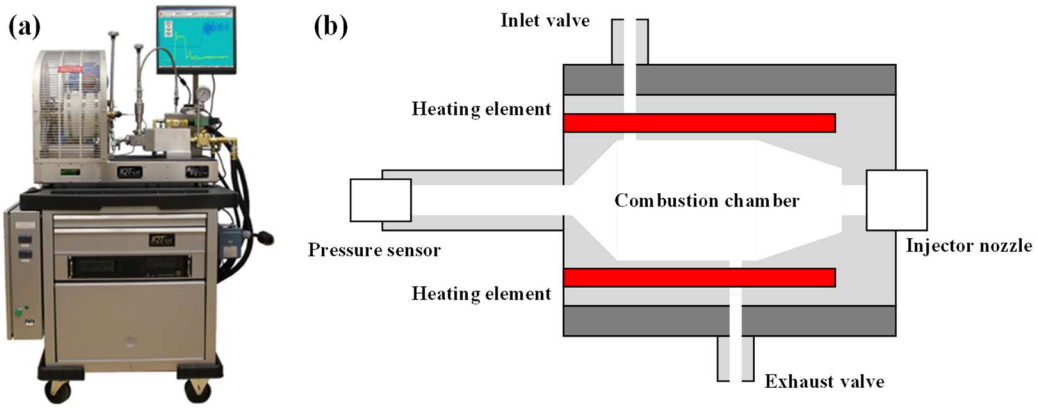

Figure 2.1. (a) Ignition Quality Tester (IQT) and (b) schematic of combustion chamber of IQT.

obtain the DCN value by measuring the ignition delay time. Figure 2.1 shows the entire system of IQT and the schematic of combustion chamber. It consists of a constant volume chamber surrounded by heater and measurement system as well as computer to recode the pressure and temperature information over the operating time. Before the fuel injection to combust, the temperature and pressure are initially maintained at 830 K 21 atm. Then, liquid fuel is injected through the fuel injector, decreasing the gas temperature and pressure inside the chamber due to the heat absorption by the liquid fuel to be vaporized. The system starts to measure the time from the fuel injection to the pressure recovery to the initial pressure. This time duration is defined as the ignition delay time in this IQT and converted to DCN through the equation $\mathrm{DCN} = 4.460 + \frac{186.6}{Ignition\ delay\ time}$ specified in ASTM D6890 [36].

2.1.2 Distillation Apparatus

Since the real fuels contains numerous components that have different physical and chemical properties, some crude oils were distilled at different temperature ranges to verify the preferential vaporization potential over the distilled cuts. Figure 2.2 shows the system to distill crude oils. It consists of the fuel reservoir, heater, cooling bath, and

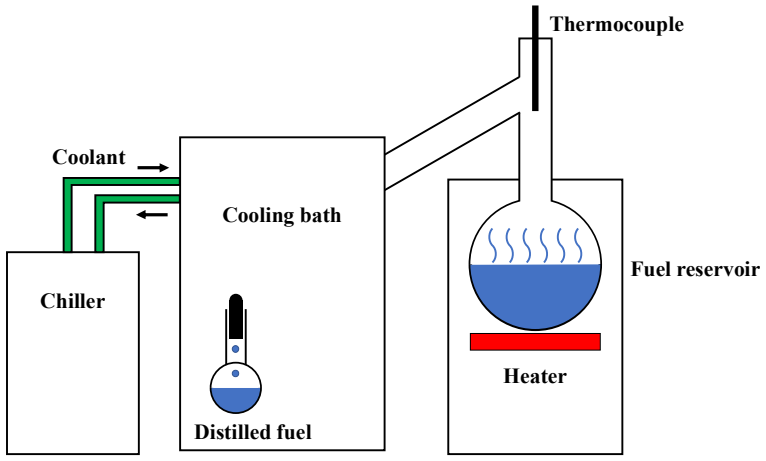

Figure 2.2. Schematic of distillation device.

container for the distilled fuel. The fuel reservoir contains the crude oils, while the heater increases the temperature of fuel reservoir slowly, which is controlled by temperature controller together with thermocouple to measure the temperature of crude oils. Then, the vaporized components by heating the reservoir move to the cooling bath to condense them into liquid. During the distillation, coolant inside the cooling bath is circulated by pump inside chiller to keep the cooling temperature constant. The distillate is taken by the container at room temperature. In this study, the crude oils were distilled at different temperature (T_b) ranges: light naphtha at $T_b < 95$ ℃, heavy naphtha at $95 < T_b < 175$ ℃, kerosene at $175 < T_b < 232$ ℃, and light gas oil at $232 < T_b < 343$ ℃. The residue for $T_b > 343$ ℃ was not used in this study due to thermal cracking at atmospheric pressure. The distillation temperature is measured at the exit to the cooling bath as following ASTM D86 procedure [37].

2.1.3 Nuclear Magnetic Resonance (NMR)

In this study, NMR is utilized to evaluate the chemical functional group distribution of fuel samples. In general, NMR is operated to measure qualitative chemical functional groups. However, when the sample is fully saturated and the time of detection is long enough to cover the relaxation time of nuclei in the fuel sample, NMR spectra can be quantitively analyzed to evaluate the fraction of chemical functional groups.

^{1}H and ^{13}C NMR spectra were obtained using a Bruker Avance III-HD 400 MHz NMR facility. NMR signal is produced by the excitation of the nuclei in the fuel sample with radio frequency into nuclear magnetic resonance, giving access to details of the individual functional groups. NMR samples were prepared by dissolving ~ 0.1 g of fuel samples into $CDCl_3$ (~ 3 cm^3) as NMR solvent with Chromium(III) acetylacetate (~ 0.15

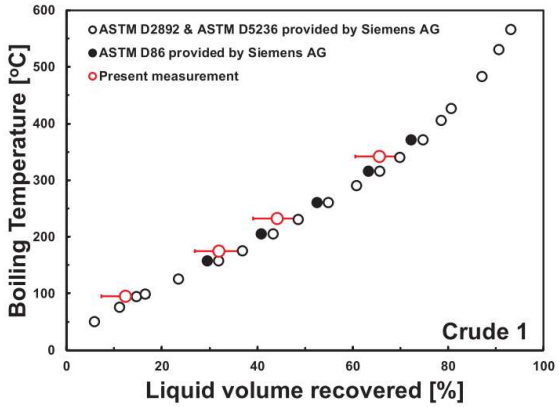

Figure 2.3. Comparison of present distillation measurements (ASTM D86) during the preparation of five distillation cut.

cm^3, $Cr(C_5H_7O_2)3$) as a relaxation agent. To obtain quantitative ^1H and semi-quantitative ^{13}C NMR spectra, sufficient long acquisition time (30 s for ^1H NMR and 40 s for ^{13}C NMR) were applied.

2.2 Preferential vaporization potential of multi-component fuels

In this study, four different crude oils (e.g., Crude 1, 2, 3, and 4) were used to observe the variation of chemical reactivity potential over vaporization temperature. Figure 2.3 compares the distillation data of Crude 1 with that reported in a crude assay. It confirms that the distillation procedures with the distillation device similarly perform to the diagnostics applied in producing the assay data.

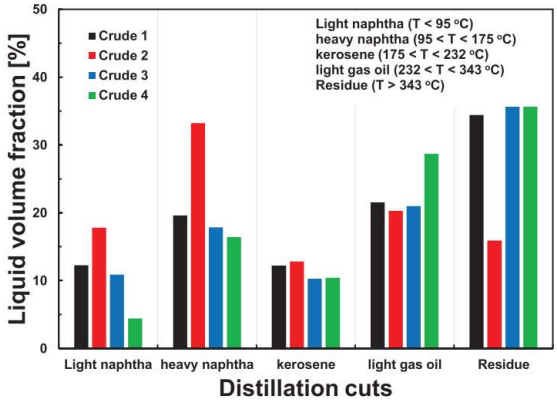

Figure 2.4. Summary of distilled liquid volume fractions from the ASTM D86 distillation device for four crude oil samples.

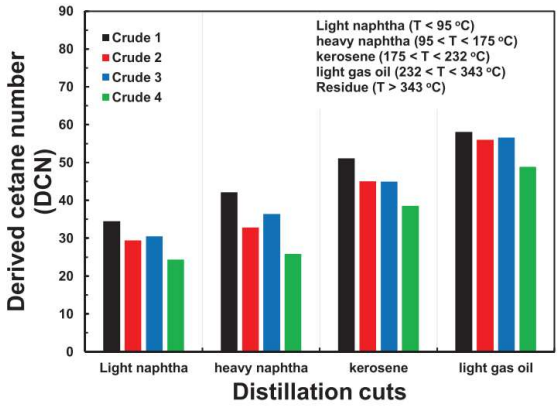

Figure 2.5. DCN values measured for the four distillation cuts of four crude oil samples.

Other crude oils are distilled at different temperature ranges. Figure 2.4 shows the liquid volume fraction of four crude oils at five different temperature ranges. Four crude oils exhibit various volume fraction at each temperature range. Crude 2, which is the lightest in this study, exhibits the largest volume fraction in light and heave naphtha ranges, while it has the smallest volume fraction in residue. On the other hand, Crude 4 has the lowest volume fraction in light naphtha range, while it has the largest volume fraction in light gas oil range. Four crude oils have similar volume fraction in kerosene range. This result indicates that multi-component fuels have different vaporization characteristics.

To investigate the chemical reactivity potential at each distillation temperature, DCN values are measured for the four distillation cuts of four crude oils. Here, the residues are not used. Figure 2.5 shows the DCN values of distillation cuts of four crude oils. The DCN value of each crude oil monotonically increases as the distilled temperature range becomes higher. Especially, at the same distillation temperature range, there exists the difference in the DCN values for four crude oils. Crude 1 has highest DCN values at each distillation temperature range, while Crude 4 has the lowest DCN

values. This result indicates that the chemical reactivity potential changes due to difference in the fuel physical property among the components in multi-component fuels.

To verify that each distillation cut is comprised of different chemicals, ^{1}H and ^{13}C NMR spectra were obtained for each distillation cuts. Figure 2.6 shows the ^{1}H NMR spectra of each distillation cuts for Crude 1. The ^{1}H NMR spectra were integrated over the chemical shift to identify the fraction of specific chemical functional group as the integrated area represents relative fraction of chemical functional groups. According to [38, 39], the range of each chemical functional group is represented in Fig. 2.6. Since ^{1}H NMR spectra do not differentiate n-paraffinic CH_2 from cycloparaffinic CH_2, ^{13}C NMR spectra is utilized to distinguish the CH_2 functional groups based on [38, 39]. Figure 2.7

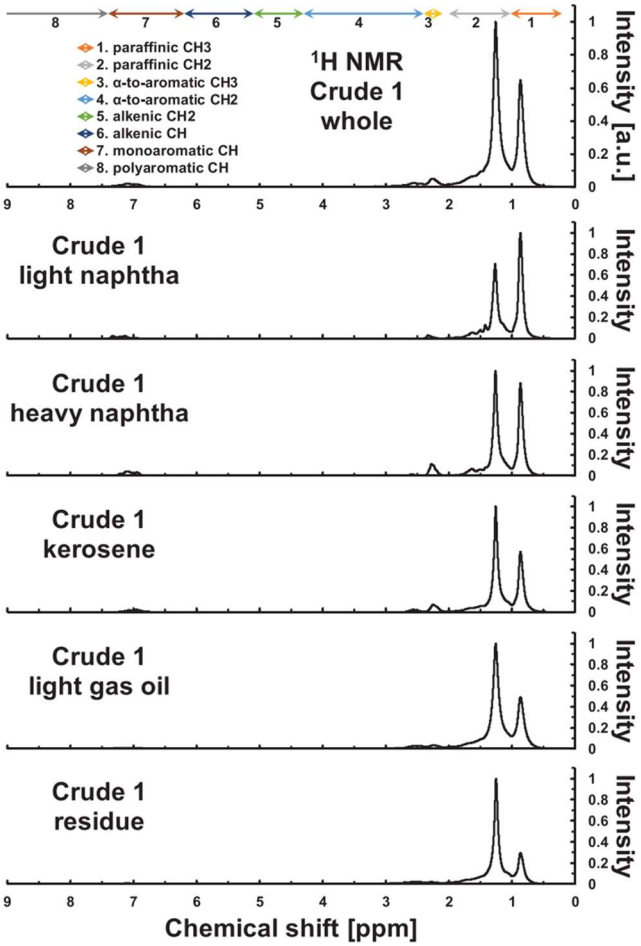

Figure 2.6. ^{1}H NMR spectra of distillation cuts of Crude 1.

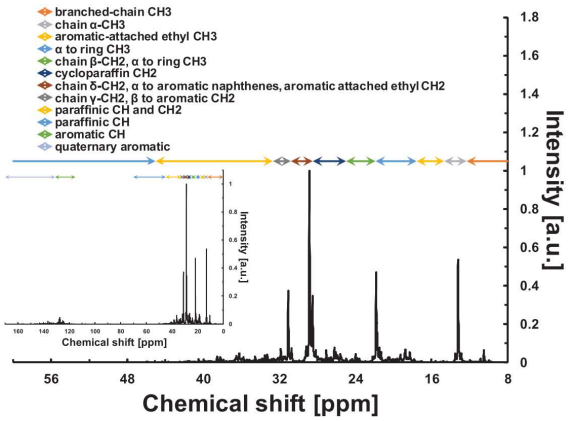

Figure 2.7. ^{13}C NMR spectra of distillation cuts of Crude 1.

shows ^{13}C NMR spectra of each distillation cuts for Crude 1 with the range of each chemical functional group.

By interpreting ^{1}H and ^{13}C NMR spectra of whole crude oil samples and their distillation cuts, mole fraction of n-paraffinic CH_2, paraffinic CH_3, and cycloparaffinic CH_2 have been quantitatively estimated. Figure 2.8 shows the estimated functional group distributions of n-paraffinic CH_2, paraffinic CH_3, and cycloparaffinic CH_2 of whole crude oils and their distillation cuts. The distillation cut number of 0 represents whole crude oil samples. The fraction of n-paraffinic CH_2 in the distillation cuts of all crude oils

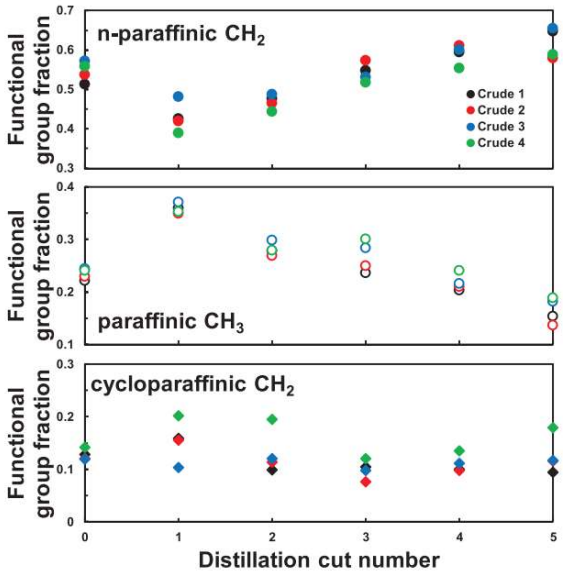

Figure 2.8. Functional group distribution of (a) n-paraffinic CH_2, (b) paraffinic CH_3, and (c) cycloparaffinic CH2 at the different distillation cuts of four crude oils.

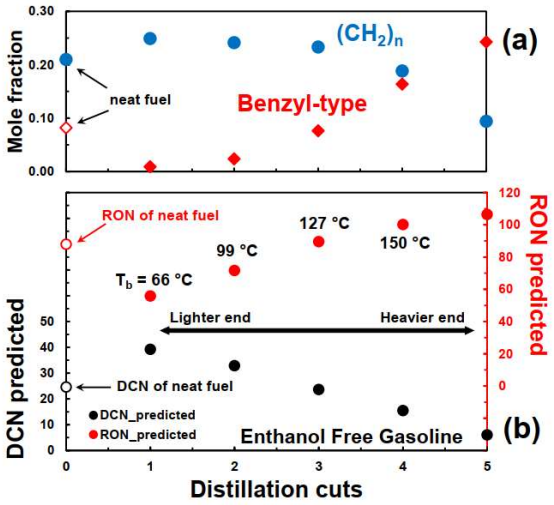

Figure 2.9. Comparison of the changes of (a) mole fractions of $(CH_2)_n$ and benzyl-type groups and (b) predicted DCN and RON values as a function of distillation cut numbers.

monotonically increases as the distillation temperature range becomes higher, while The fraction of paraffinic CH_3 decreases. On the other hand, cycloparaffinic CH_2 is contained in the distillation cuts with the small variation in the functional group distribution. Considering that n-paraffinic CH_2 contributes to boosting the chemical reactivity potential, while paraffinic CH_3 deteriorates the chemical reactivity potential, qualitative analysis based on the NMR spectra is well agree with higher DCN values of distillation cuts at higher distillation temperature range as shown in Fig. 2.5.

Additionally, the change in the chemical reactivity potential of ethanol free gasoline was observed in the same manner. Figure 2.9 shows the mole fraction n-paraffinic CH_2, benzyl-type group, and predicted RON and DCN as a function of distillation cut numbers. The DCN values were predicted based on methodology presented in previous work [18, 40, 41]. The mole fraction of n-paraffinic CH_2 slowly decreases until the boiling temperature of 127 °C, and then drastically decreases. On the

other hand, the fraction of benzyl-type group monotonically increases. Therefore, the predicted DCN value decreases as the distillation temperature becomes higher.

The result in this chapter confirms that the chemical reactivity potential varies as a function of distillation temperature. This indicates that the preferentially vaporized fuel components from multi-component liquid fuels will play a considerable role in controlling the combustion behaviors such as flame flashback and flame extinction, which are sensitive to the chemical kinetic characteristic of fuel composition

CHAPTER 3

IMPACT OF PREFERENTIAL VAPORIZATION ON FLAME FLASHBACK

Compared to the Rich-Burn, Quick-Quench, Lean-Burn combustor, the Lean-Premixed Prevaporized combustor typically incorporates a premixer (mixing tube), thus requiring a careful design to avoid flame flashback [42]. Extensive investigations have been performed to characterize the flashback behaviors (e.g., [43-48]). Five feasible flashback mechanisms are well summarized in [46] for gas-phase combustion phenomena: flashback by autoignition, flashback in boundary layers, turbulent flame propagation in the core flow, combustion instability leading to flashback, and flashback induced by vortex breakdown. These flashback mechanisms were established at given gas phase fuel compositions without involving spray dynamics. However, for partially vaporized fuel/air mixtures, little consideration has been given to how fuel physical/chemical properties might combine to affect local chemical kinetic reactivities other than local equivalence ratio determination.

The objective of this study is to investigate and evaluate the relative significance of preferential vaporization on flame flashback relevant to multi-component fuels. A spray burner is developed, including a movable fuel injector to control the extent of fuel vaporization. To evaluate the relative significance of preferential vaporization, two different mixtures, each sharing the same chemical functional group distributions, but

having different chemical reactivity potentials during their evaporation, are formulated and tested in the spray burner. At the near-fully vaporized conditions achieved by setting the burner temperature at 700 K, the flame flashback behaviors are investigated first to ensure that the formulated two mixtures share the same chemical kinetic reactivity. Two distinct flashback modes, propagation- and autoignition-driven flashback, which are related primarily to chemical reactivity, are then examined for the two fully vaporized cases.

By setting the burner temperature at 450 K to achieve partially vaporized conditions, the impact of preferential vaporization on flame flashback are examined at two different global equivalence ratios. To fruitfully evaluate the preferential vaporization impact, Phase Doppler Particle Analyzer (PDPA) measurements are simultaneously analyzed, allowing the characterization of effective equivalence ratio and local flow velocity fluctuations on the partially vaporized conditions. Finally, the relative significance of preferential vaporization is discussed in terms of local laminar flame speeds based on effective equivalence ratios and local flow velocity fluctuation that affect the overall burning rates. These characteristics are examined through a Markstein number analysis based upon planar laser-induced fluorescence (PLIF) imaging.

3.1 Experimental methodology

3.1.1 Experimental Apparatus

To investigate the impact of fuel vaporization on flame flashback characteristics, a spray burner has been developed, which can control the extent of liquid fuel evaporation. The experimental configuration is schematically illustrated in Fig. 3.1. To obtain a top-hat velocity profile at the exit of the nozzle, a converging section reducing

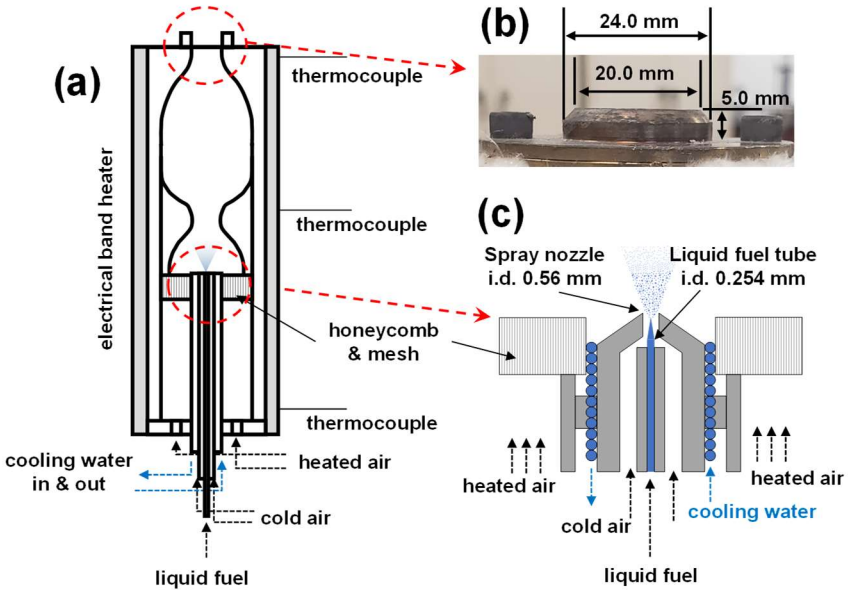

Figure 3.1. (a) Schematics of spray burner, (b) direct photo at the nozzle exit, and (c) schematics of movable spray injector.

the internal diameter from 50 mm to 20 mm with 75 mm in length is located. The nozzle diameter is 20 mm. Air is supplied from the bottom of the burner after passing through the electric heater, which is controlled by a PID controller to keep the air temperature constant. The entire burner is heated by an electric band heater, which is also controlled through a PID controller by measuring the temperature with K-type thermocouples at three locations as indicated in Fig. 3.1(a).

To achieve a reliable spray pattern, an air-blast spray injector was built, as described schematically in Fig. 3.1(c). Liquid fuel is injected through a central nozzle (0.254 mm inner diameter) surrounded a coaxial outer tube with an exit inner diameter of 0.56 mm. The airflow introduced into the air-blast spray injector through the outer tube is maintained constant at 0.6 L/min throughout all measurements to minimize the changes in spray pattern. To avoid fuel vaporization inside the fuel injector and the potential change of physical properties of the liquid fuel (e.g., cavitation), cooling water is circulated inside the injector body to maintain the liquid fuel temperature at 300 K. The

entire body of the air-blast spray injector is surrounded by a honeycomb structure to ensure heated airflow uniformity entering the burner. Above the honeycomb structure, a converging-diverging section (150 mm in length and 20 mm throat diameter) is located to produce uniform spray/droplet distribution characteristics. The entire injector body (including the honeycomb structure and the converging-diverging section) is designed to be moved vertically. Thus, the flow residence time inside the burner can be controlled to vary the extent of fuel spray vaporization. Here, the flow residence time is defined by the volume of the vaporization section and the volumetric flow rate of fuel and air mixture.

Airflow rates are controlled by mass flow controllers (Brooks Instrument, SLA5850) and sonic nozzles calibrated with a DryCal 800 (Mesa Labs) at room temperature. Liquid fuel is delivered by a high-pressure syringe pump (Harvard Apparatus, PHD 2000). The reported volumetric flow rate refers to the sum of fully vaporized fuel and air volumetric flow rates. Since the fraction attributed to the liquid fuel flow rate is smaller than 2% of the total flow rate (for the equivalence ratio conditions tested here), the partially vaporized conditions can be reasonably well estimated within the uncertainties of flow controllers used regardless of the extent of liquid fuel vaporization.

Direct images of premixed Bunsen flames are taken with a digital camera (Nikon, D3400). To monitor the dynamics of ignition-driven flashback behavior, a series of Schlieren images using a LED light source (Thorlabs, M530L3) is taken with a high-speed camera (Photron, SA-Z). Flame structures as a function of the extent of fuel vaporization are also monitored by employing PLIF imagining for OH radical. A frequency-doubled Nd:YAG laser (Spectra-Physics, Quanta-Ray Pro-250-10) pumps a

Dye laser (Spectra-Physics, Cobra-Stretch) with Rhodamine 590 to generate the excitation frequency for the $Q_1(6)$ OH transition (~283 nm, 6 mJ/pulse). The beam is spread and focused into a sheet (~ 150 μm thick and ~ 60 mm tall) by using a cylindrical lens and a plano-convex lens and directed across the center of the burner. The fluorescence image is captured by an Intensified CMOS camera (Andor, iStar sCMOS) with a 100 mm f/2.8 UV lens (Cerco) and two bandpass filters (UG-11 and WG-305).

To characterize the spray properties, the droplet size and velocity distributions are measured using a Phase Doppler Particle Analyzer (PDPA, TSI). A single component fuel, n-dodecane (nC12) supplied at a global equivalence ratio of unity, was used to test partial vaporization operation at a burner temperature of 400 K. The spray burner developed is an adaptation of the design concept reported in [49, 50], developed to achieve near-homogenous droplet and velocity distributions at the nozzle exit. To confirm these behaviors, droplet size and velocity distributions were measured radially by PDPA at 3 mm above the nozzle exit. Figure 3.2(a) shows the radial distributions of the arithmetic mean diameter (d_{10}), surface mean diameter (d_{20}), and volume mean diameter (d_{30}) at the mean jet velocity (U_0) of 240 cm/s. Figure 3.2(b) depicts the radial profiles of the mean velocity and local velocity fluctuation (u') determined from the standard deviations of the PDPA measurements. The measured mean velocities by PDPA agree with the mean jet velocity based on volumetric flow rate within 2 % uncertainty. Considering the Stokes number calculated based on the measured droplet diameter and burner nozzle diameter is < 0.1, the velocity measurements by PDPA can be regarded as the flow velocity and its fluctuation [51].

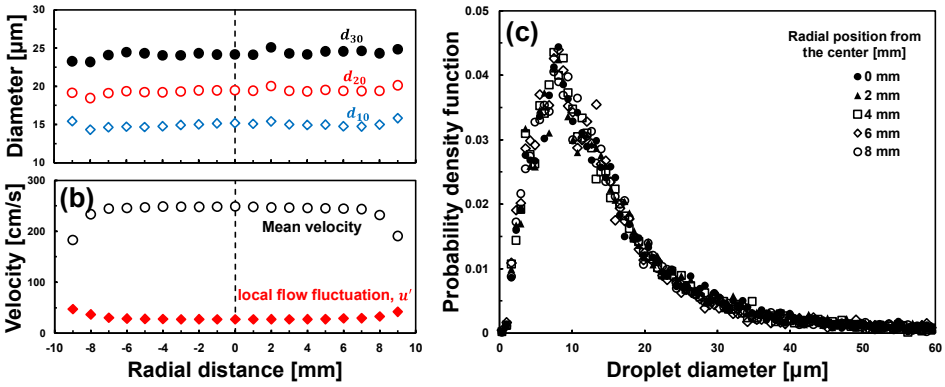

Figure 3.2. (a) Radial distributions of three droplet sizes, Arithmetic mean diameter (d_{10}), Surface mean diameter (d_{20}), and Volume mean diameter (d_{30}) measued by PDPA at U_0 = 240 cm/s for stoichiometric n-dodecane/air mixture at 400 K. (b) Radial profiles of the mean velocity and local velocity fluctuation (u') defined from standard deviation measured by PDPA. (c) Distributions of droplet diameters for various radial positions at 3 mm above nozzle exit.

Figure 3.2(c) shows the measured droplet size distribution at various radial positions, exhibiting near-identical characteristics regardless radial position. Near-constant values of d_{10}, d_{20}, and d_{30} in Fig. 3.2(a) and near-identical droplet size distribution along the radial direction suggest that droplet size distributions are uniform, assuring that measurements at the center of the nozzle flow are accurate representations of the spray characteristics.

Subsequently, the droplet size distributions with changing flow residence time (extent of vaporization) are characterized by PDPA measurements at the center of the burner exit. Flow residence time (τ_{res}) is controlled by changing fuel and airflow rates, as well as moving the injector location. Here, we use volume mean diameter (d_{30}) instead Sauter mean diameter (d_{32}), to properly evaluate the extent of fuel vaporization based on volumetric fuel flow rates.

Figure 3.3(a) shows the squared values of the measured d_{30} as a function of τ_{res}. In the case of fuel vaporization in spray, the rate of fuel vaporization is known to be

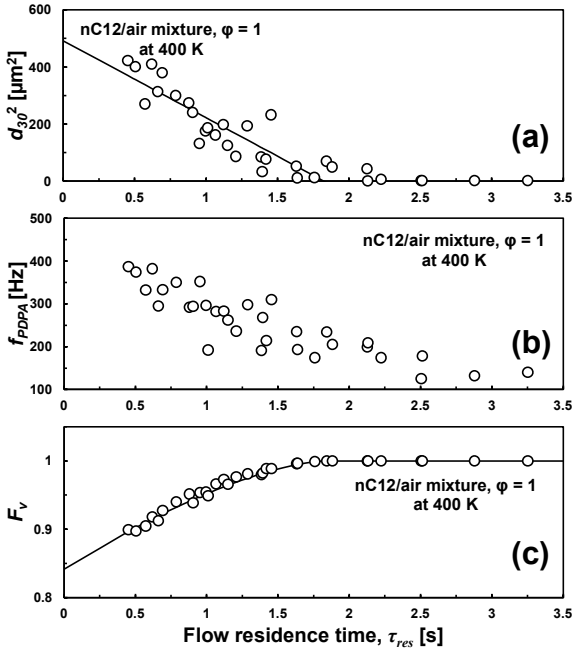

Figure 3.3. Summary of PDPA measurements at the nozzle exit for stoichiometric n-dodecane/air mixture at 400 K as a function of flow residence time (τ_{res}); (a) the squared values of the measured d_{30} as a function of τ_{res}, (b) the measured PDPA sampling frequency (f_{PDPA}) as a function of τ_{res}, and (c) the calculated vaporized fuel fraction as a function of τ_{res}.

governed through the complicated interactions among the spray droplets [52, 53]. Nevertheless, the theoretical analyses suggest that the rate of fuel droplet vaporization follows the typical D^2 law for a single droplet, once the distances between the droplets are sufficiently large [52, 53]. Based on the volumetric flow rate and the measured d_{30} as well as the sampling frequency of PDPA measurement (f_{PDPA}), the mean distance among fuel droplets are estimated ten times larger than d_{30} (>10d_{30}), supporting the observed moderate linear trend of ${d_{30}}^2$ as a function of τ_{res}. When τ_{res}>3 s, the measured d_{30} becomes smaller than 2 μm, comparable to the PDPA measurement limit (~ 1 μm), indicative of reaching a fully vaporized condition.

The increased extent of fuel vaporization with τ_{res} can be also seen from the sampling frequency in PDPA measurements (f_{PDPA}), as shown in Fig. 3.3(b), which

monotonically decreases as increasing τ_{res}. The volume fraction of fuel vaporized (F_v) can be determined by incorporating the measured d_{30} and f_{PDPA} in the following equation.

$$F_v = 1 - \frac{\pi {d_{30}}^3}{6Q_{Fuel}} \frac{A_{nozzle}}{A_{PDPA}} f_{PDPA} \qquad \text{(Eq. 3.1)}$$

Here, A_{nozzle} and A_{PDPA} are the area of the burner exit and the cross-sectional area of the sampling volume of the PDPA, respectively. Here, A_{nozzle} is calculated based on the nozzle diameter and A_{PDPA} is estimated based on the laser beam alignment as described in the TSI operations manual. The two identical laser beams from the PDPA cross at the measurement volume bounded by the ellipsoidal surface, which is the surface that the light intensity of fringe is $1/e^2$ of the maximum intensity. With the given half-angle (θ) between two laser beams and laser diameter ($D_{e^{-2}}$), A_{PDPA} is $4f^2\lambda^2/\pi {D_{e^{-2}}}^2 \sin\theta$. Here, f and λ are the focal length of the lens in PDPA and laser wavelength, respectively. Q_{Fuel} is total fuel flow rate into the spray burner.

Figure 3.3(c) shows the estimated volume fraction of fuel vaporized (F_v) as a function of τ_{res}. The solid line is derived from fitting into the following equation by varying $d_{30,initial}$.

$$F_v = 1 - \left(\frac{d_{30}}{d_{30,initial}}\right)^3 \qquad \text{(Eq. 3.2)}$$

The initial d_{30} values ($d_{30,initial}$) estimated from Eq. 3.2 is 41 μm, which is different from the estimation from the linear extrapolation on the observed moderate linear trend of ${d_{30}}^2$ (~24 μm). This difference can be attributed to the existence of the converging-diverging section to achieve uniform distribution of spray droplets inducing local flow acceleration, therefore reducing the dynamic pressure resulting in accelerating the fuel vaporization. Nevertheless, the results shown in Fig. 3.3 confirm that the extent of fuel vaporization

can be controlled by changing the mean flow rate and/or the injector location that governs the flow residence time.

3.1.2 Formulation of binary component test mixtures

Combustion behaviors of partially vaporized fuel/air mixtures inevitably involve complicated coupling impacts between fuel physical and chemical properties. Recent experimental observations of LBO with petroleum-derived jet fuels, alternative jet fuels, and their blends suggest that the impact of fuel chemical property may also be significant [13-16]. The significant role of fuel chemical property appeared through a strong correlation of LBO with the derived cetane number (DCN) of fuel that represents the chemical reactivity potential [12, 18, 54, 55].

Knowing that the impact of preferential vaporization on near-limit combustion behaviors appears through complicated interactions, two binary component mixtures were specifically formulated based on our previous works [18, 27-29, 55-57] to simplify the analysis. Mixture 1 is composed of n-octane (nC8) and iso-cetane (iC16) and Mixture 2 is composed of iso-octane (iC8) and n-hexadecane (nC16), as summarized in Table 3.1. The mixture compositions were optimized to achieve a similar DCN value of n-heptane (53.8), thus exhibiting a similar chemical reactivity potential. In the case of n-alkane/iso-

Table 3.1. Summary of two binary component mixtures formulated by matching key chemical functional group distribution.

	Mixture 1 (nC8/iC16)	Mixture 2 (iC8/nC16)
n-octane (nC8)	0.74	0
iso-octane (iC8)	0	0.67
n-hexadecane (nC16)	0	0.33
iso-cetane (iC16)	0.26	0
Calculated DCN	53.4	53.6
$(CH_2)_n/CH_3$ molar ratio	1.16	1.15

alkane mixtures, the overall chemical kinetic characteristics of these fuels are primarily governed by the ratio of methylene (CH_2) and methyl (CH_3) functionalities [55]. The relative contributions of CH_2 and CH_3 functionalities on global combustion behaviors were further contrasted by introducing a methylene chain, $(CH_2)_n$ ($n \geq 3$), which not only governs the low-temperature chain branching reactions but also reflects high-temperature reactivities, as discussed in [18, 56]. The two mixtures also share very similar values of the $(CH_2)_n$ to CH_3 molar ratio, therefore it is expected to exhibit identical chemical kinetic reactivities in both high- and low-temperature combustion regimes.

Though these two binary component mixtures have identical global combustion behaviors for fully vaporized conditions, their combustion behaviors are expected to differ when preferential vaporization is important. To evaluate this difference, the fuel

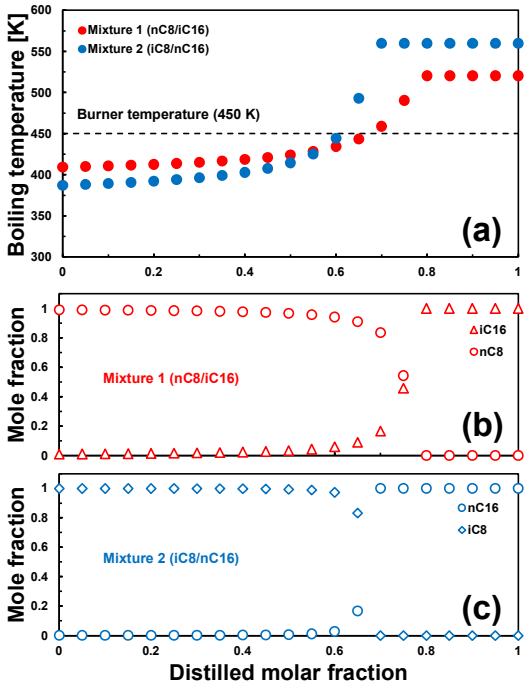

Figure 3.4. (a) Boiling temperatures of two binary component mixtures with distilled molar fraction, (b) mole fractions of nC8 and iC16 with distilled molar fraction for Mixture 1, and (c) mole fractions of iC8 and nC16 with distilled molar fraction for Mixture 2.

boiling temperatures and local gas-phase compositions are calculated as a function of distilled molar fraction as shown in Fig. 3.4. The approach to calculate the fuel distillation curve can be found in [18, 58]. Although the two mixtures are formulated with the same carbon numbers (C8 and C16), the difference in boiling temperatures between nC8 and iC8 results in a slightly higher initial boiling temperature for Mixture 1 due to the slightly higher boiling temperature of nC8 than that of iC8 (Fig. 3.4(a)). Similarly, due to the lower boiling temperature of iC16 than that of nC16, the final boiling temperature of Mixture 1 is slightly lower than that of Mixture 2.

Fuel composition in gas phase from vaporizing mixtures changes over fuel vaporization process due to the difference in the boiling temperature between the components in the mixtures. In the case of Mixture 1 shown in Fig. 3.4(b), the lighter component, nC8 evaporates earlier than the heavier component iC16, thus depositing a relatively reactive component in the gas phase. However, iC8 evaporates earlier in the case of Mixture 2 (Fig. 3.4(c)), which has lower chemical reactivity compared to nC8 in Mixture 1. Therefore, it is expected that Mixture 1 will have a higher reactivity (e.g.,

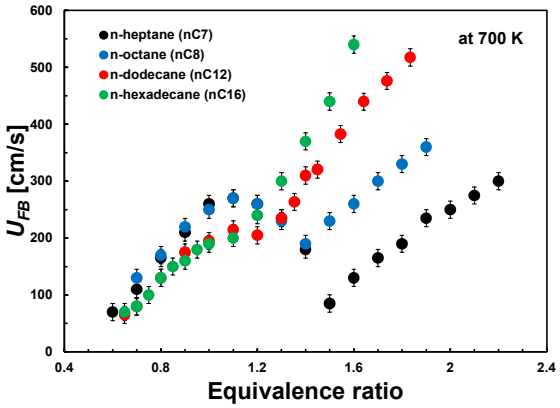

Figure 3.5. Measured U_{FB} as a function of global equivalence ratio (φ_g) for four n-alkanes, n-heptane (nC7), n-octane (nC8), n-dodecane (nC12), and n-hexadecane (nC16) at 700 K (fully vaporized condition).

laminar flame speed, ignition propensity) than Mixture 2 when the preferential vaporization occurs.

3.2 Flame flashback behaviors in fully vaporized condition

Prior to the experiments for partially vaporized conditions, the flame flashback behaviors in the fully vaporized conditions are investigated by setting the burner temperature at 700 K. To determine flame flashback conditions, a stable flame at relatively higher mean jet velocity is firstly established at the exit of the nozzle. Then, the mean jet velocity is gradually reduced until the flame base suddenly penetrates inside the burner. When flame flashback occurs, the mean jet velocity (U_0) is assigned as U_{FB}. Figure 3.5 shows the measured U_{FB} as a function of global equivalence ratio (φ_g) for four n-alkanes, n-heptane (nC7), n-octane (nC8), n-dodecane (nC12), and n-hexadecane (nC16). As clearly depicted in Fig. 3.5, there are two distinct regimes for n-alkanes, propagation-driven flashback at relatively lean equivalence ratios and ignition-driven flashback at relatively rich equivalence ratios. Those two different flashback modes are distinguished by observing how the flashback occurs. When the burning rate of flame is faster than volumetric flow rate of gas mixture, the propagation-driven flashback occurs by the flame propagating back to the inside of the burner. On the other hand, the ignition-driven flashback happens with the autoignition of mixture, creating the flame inside the burner.

While the propagation-driven flashback is primarily controlled by laminar flame speed and diffusive characteristics [59, 60], the ignition-driven flashback is controlled by the onset of autoignition as discussed previously elsewhere [61, 62]. The onset global equivalence ratios of n-alkanes become leaner as increasing the molecular weight of n-

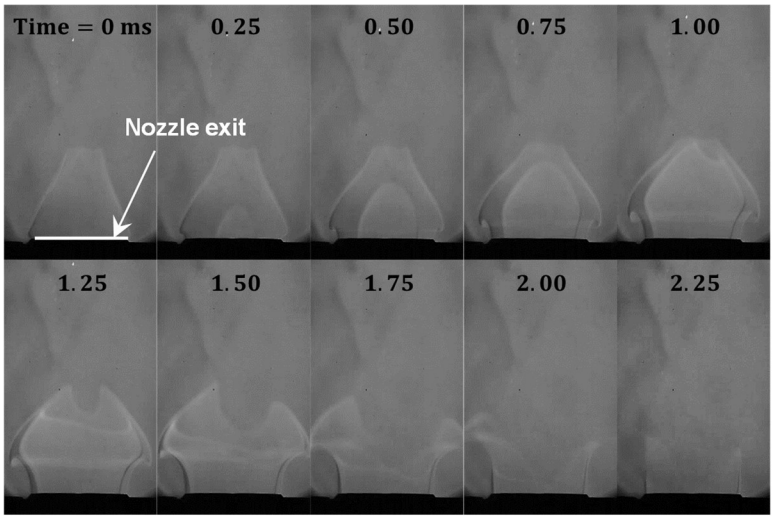

Figure 3.6. Time series of Schlieren images for n-dodecane at the global equivalence ratio, $\varphi_g = 1.4$, $U_0 = 280$ cm/s for ignition-driven flashback behaviors. Nozzle exit is marked with a white line.

alkane (the length of CH_2 backbone), 1.5 for nC7, 1.4 for nC8, 1.3 for nC12, and 1.2 for nC16, inversely proportional to their DCN values [63]. Since the flow residence time (τ_{res}) inside the burner is inversely proportional to U_{FB}, the results suggest that the autoignition delay time becomes shorter as the chain length of the CH_2 backbone in n-alkanes is increased. This trend is qualitatively identical to the predicted and measured dependency of homogenous reflected shock ignition delay times in terms of n-alkane chain length and equivalence ratio [1, 55, 64-67].

Figure 3.6 shows the time series of Schlieren images for n-dodecane at the global equivalence ratio ($\varphi_g = 1.4$ and $U_0 = 280\ cm/s$). Initially (at $t = 0\ ms$), the Schlieren image clearly shows a typical Bunsen premixed flame attached to the nozzle exit represented by a sharp density gradient. Similar to the previous work [62], the autoignition kernel appears at the nozzle exit at 0.25 ms, indicating that autoignition occurs at the given flow residence time, thus inducing the ignition-driven flashback. The autoignition kernel continues grow and merges with the premixed flame at ~ 1.25 ms.

Then, the entire flame starts penetrating into the burner exit, eventually completing the flashback sequence at ~ 2.25 ms, where no discernible flame structure can be seen.

The transitions to ignition-driven from propagation-driven flashbacks in Fig. 3.5 are demarcated clearly for nC7 and nC8, while those of nC12 and nC16 are found to occur smoothly as a function of φ_g. These results can be attributed to the mechanistic behaviors of the two-stage ignition process in low-temperature conditions. Both the first- and second-stage ignition delay times become shorter with increasing the length of CH_2 backbone in n-alkanes and the interval between the first- and second-ignition delay times also become shorter with increasing equivalence ratio [67-69]. Thus, the fast transition to the second-stage ignition at rich conditions renders more abrupt and distinct transition to the ignition-driven flashback for nC7 and nC8. Relatively smooth transitions found for nC12 and nC16 can be attributed to the excessive heat release after the first-stage ignition that affects the transition to the second-stage ignition. Although not specifically measured during the experiments, the temperature measurement at the nozzle exit exhibits a continuous increase approaching ~ 80 K over the setpoint (700 K), coinciding with the onset of ignition-driven flashback. Heat loss occurs inside the burner after the onset of

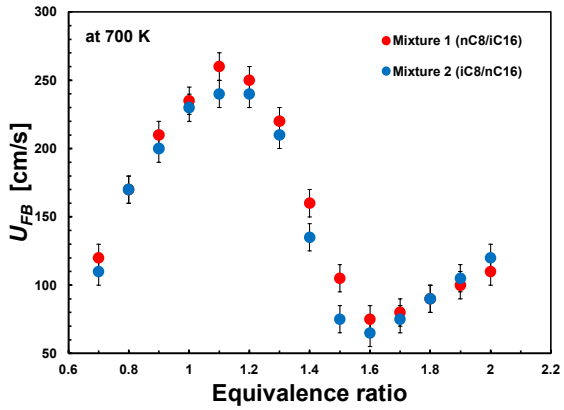

Figure 3.7. Comparison of the measured U_{FB} values of two binary component mixtures at fully vaporized condition a 700 K of the burner temperature as a function of equivalence ratio.

the first-stage ignition, thus lowering the global burning rate and the measured U_{FB}, compared to nC7 and nC8. Chemical kinetic characteristics associated with heat loss after the first-stage ignition have been discussed previously in [62], and further characterization and discussion here is beyond the scope of the present investigation.

Figure 3.7 compares the measured U_{FB} values of two binary component mixtures at fully vaporized condition with 700 K of the burner temperature. Within measurement uncertainty, the two mixtures exhibit almost identical flashback behaviors for both propagation- and ignition-driven flashback regimes. This result confirms the effectiveness of the mixture formulation by matching the key chemical functional group distributions as shown in Table 3.1. It suggests that the flashback behaviors of the two mixtures will be similar at the near-fully vaporized conditions. It also implies that results will differ under preferentially vaporizing conditions due to the difference of laminar flame speed caused by the composition difference shown in Fig. 4, which governs the propagation-driven flashback behaviors [43-48].

3.3 Flame flashback behaviors in partially vaporized condition

Confirming the commonality of flashback behaviors of two binary component mixtures once they are fully vaporized, the potential impacts of preferential vaporization on flame flashback are investigated at a partially vaporized condition. The burner temperature is reduced from 700 K to 450 K based on the calculated distillation behaviors of two mixtures as shown in Fig. 3.4.

Before testing the binary component mixtures, flame behaviors as a function of flow residence time were observed for n-dodecane. Figure 3.8 shows direct photos (top) and Schlieren images (bottom) of n-dodecane flames at $\varphi_g = 1$ and $U_0 = 280\ cm/s$ by

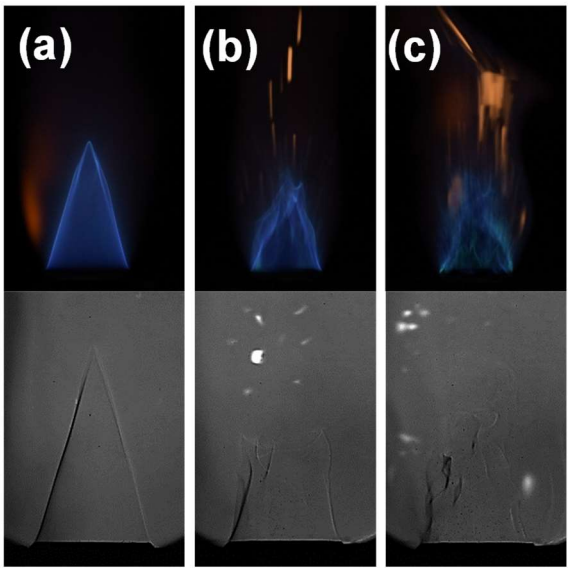

Figure 3.8. Direct photos (top) and Schlieren images (bottom) of n-dodecane flames at $\varphi_g = 1$ and $U_0 = 280$ cm/s by varying the flow residence time (τ_{res}) at 450 K. (a) $\tau_{res} = 1.22$ s, (b) $\tau_{res} = 0.54$ s, and (c) $\tau_{res} = 0.32$ s.

varying the flow residence time (τ_{res}) at various injector positions. At $\tau_{res} = 1.22\ s$, a stable Bunsen premixed flame can be observed (Fig. 3.8(a)), indicating that τ_{res} is long enough to fully evaporate the atomized liquid n-dodecane spray inside the burner. By reducing τ_{res} to 0.54 s (Fig. 3.8(b)), an unstable Bunsen premixed flame was observed. As the extent of fuel vaporization is further reduced by shortening τ_{res} to 0.32 s, the flame structure is significantly perturbed, as shown in Fig. 3.8(c). The perturbation of flame structures at the partially vaporized conditions can be attributed primarily to the local flow velocity fluctuation that has a strong correlation with the extent of fuel vaporization (shown in Figs. 3.9(d) and 3.10(d)). Instantaneous vaporization of fuel droplets near the flame surface induces convective flow perturbation through the interaction between Stefan flow and the density difference during the phase change [70, 71]. Further details are discussed later with PLIF images.

To further elaborate upon the role(s) of preferential vaporization on flame flashback behaviors, the images shown in Fig. 3.8 suggest that two other impacts should

be considered carefully. First, it is necessary to determine the extent of fuel vaporization, which defines the deposition of gas phase fuel before the flame front. When the injected liquid droplets are partially vaporized, the vaporized fuel mixed with air determines the local effective equivalence ratio, which would control the overall burning rate of flames, therefore the onset of flashback. The other is the influence of local velocity perturbation caused by the instantaneous vaporization of fuel droplets when the fuel droplets before/after entering the flame preheat zone. The local flow velocity perturbation results in wrinkling of the flame structure, increasing the overall burning rate by increasing the effective flame surface area. To quantify and evaluate the contributions from these two physics, spray properties were systematically measured by PDPA at 3 mm above the nozzle exit, which determines the droplet diameter (d_{30}) and the local flow perturbation (u') simultaneously.

Figure 3.9(a) shows the measured d_{30} values for both binary component mixtures at the global equivalence ratio of 1.0 ($\varphi_g = 1$) as a function of flow residence time (τ_{res}). While the measured d_{30} values of Mixture 1 exhibit a monotonically decreasing trend, those of Mixture 2 exhibit relatively constant values. This can be attributed to the difference in boiling temperatures between nC16 and iC16, which are 554 K and 513 K, respectively. Although the measured d_{30} values for Mixture 2 do not change much, the measured PDPA frequency (f_{PDPA}) decreases considerably with τ_{res}, suggesting that the lighter component in Mixture 2 (iC8) continuously evaporates from the fuel droplets. Combining the results in Figs. 3.9(a) and (b), the extent of fuel vaporization can be estimated by using Eq. 3.1. Figure 3.9(c) shows the vaporized fraction (F_v) as a function of τ_{res}, demonstrating that the extent of fuel vaporization increases as increasing τ_{res}.

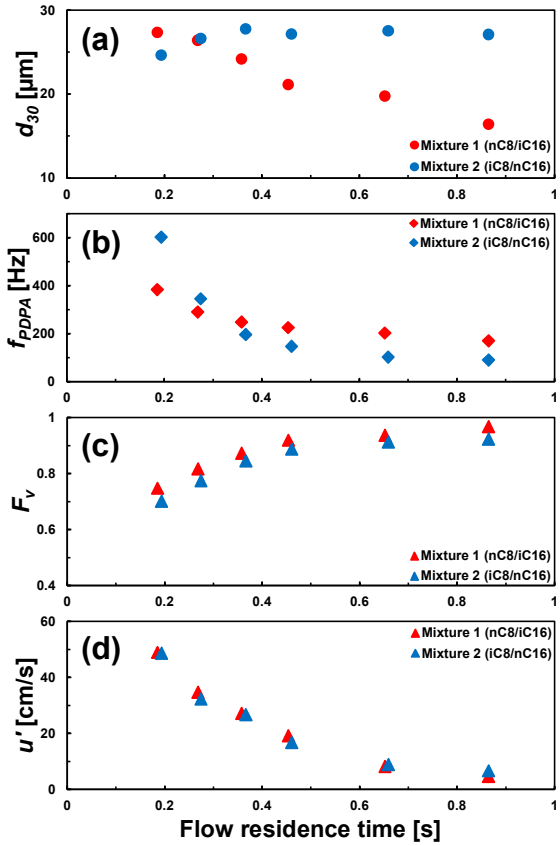

Figure 3.9. Summary of PDPA measurements for two mixtures at $\varphi_g = 1.0$ as a function of τ_{res} at 450 K; (a) the measured d_{30} values, (b) the measured PDPA sampling frequency (f_{PDPA}), (c) the calculated vaporized fuel fraction, and (d) local velocity fluctuation (u').

The estimated F_v value allows calculating the local effective equivalence ratio ($\varphi_{effective}$). The calculated $\varphi_{effective}$ of Mixture 1 varies from 0.73 to 0.97 with increasing τ_{res}, and from 0.68 to 0.92 with Mixture 2. To evaluate the local flow velocity perturbations, the standard deviations of the measured droplet velocities by PDPA are shown in Fig. 3.9(d). The average values of droplet velocities (not shown) coincided with the mean jet velocities to within measurement uncertainties (< 5%).

Figure 3.10 summarizes the results of PDPA measurements for the two mixtures at $\varphi_g = 1.4$. Compared to the results at $\varphi_g = 1$, the measured d_{30} values are slightly smaller due to the increase of fuel flow rate at the injector, which enhances the formation

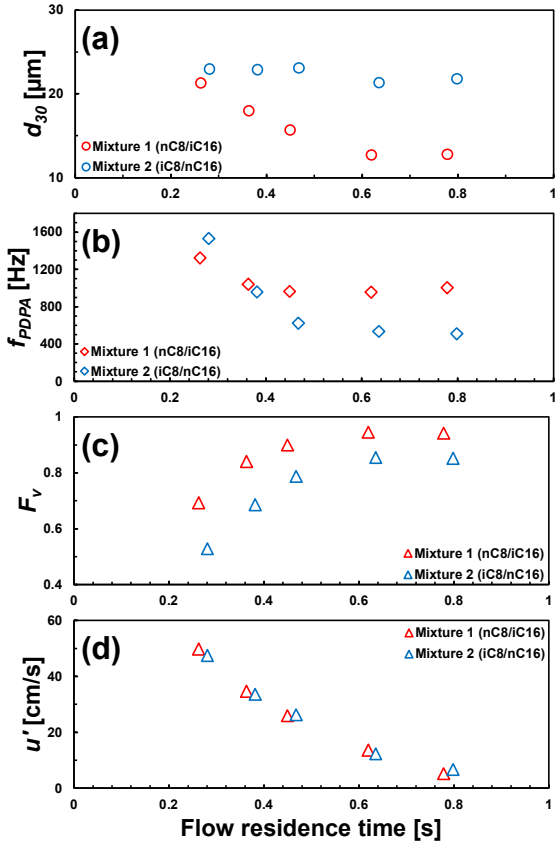

Figure 3.10. Summary of PDPA measurements for two mixtures at $\varphi_g = 1.4$ as a function of τ_{res} at 450 K; (a) the measured d_{30} values, (b) the measured PDPA sampling frequency (f_{PDPA}), (c) the calculated vaporized fuel fraction, and (d) local velocity fluctuation (u').

of fine spray droplets. The estimated vaporized fraction in Fig. 10(c) shows that Mixture 1 approaches the near-fully vaporized condition at large τ_{res}, whereas Mixture 2 does not achieve a fully vaporized condition in the range of τ_{res} investigated in this study. Accordingly, the calculated $\varphi_{effective}$ varies with increasing τ_{res} from 0.94 to 1.32 for Mixture 1 and from 0.70 to 1.18 for Mixture 2.

The changes of the effective surface burning area due to the local flow perturbation from droplet vaporization were evaluated by taking OH PLIF images of two mixtures as a function of τ_{res} by adjusting the fuel injector location at the fixed $U_0 = 280\ cm/s$. In general, no considerable differences in flame surface wrinkling were

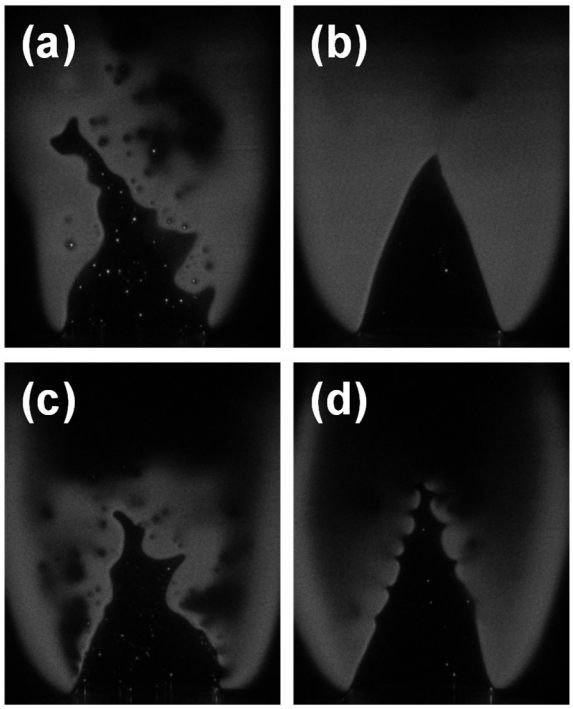

Figure 3.11. Representative OH PLIF images at 450 K; (a) Mixture 1 at $\varphi_g = 1.0$ and $\tau_{res} = 0.22$ s, (b) Mixture 1 at $\varphi_g = 1.0$ and $\tau_{res} = 0.70$ s, (c) Mixture 2 at $\varphi_g = 1.4$ and $\tau_{res} = 0.22$ s, and (d) Mixture 2 at $\varphi_g = 1.4$ and $\tau_{res} = 0.70$ s.

observed between Mixture 1 and Mixture 2, regardless of φ_g and τ_{res}. Figures 3.11(a) and 3.11(b) show the flame structures of Mixture 1 for $\varphi_g = 1$ at $\tau_{res} = 0.22\ s$ and 0.70 s, respectively. Compared to the near-fully vaporized condition at $\tau_{res} = 0.70\ s$, which exhibits a typical premixed Bunsen flame, the OH PLIF image at $\tau_{res} = 0.22\ s$ clearly shows pronounced flame surface wrinkling. Multiple local regions having no OH LIF signals are observed just downstream of the flame surface, which are induced by the instantaneous evaporation of fuel droplets as they pass through the flame surface. In the case of $\varphi_g = 1.4$, the OH PLIF image at $\tau_{res} = 0.22\ s$ in Fig. 3.11(c) also shows pronounced flame surface wrinkling similar to that in Fig. 3.11(a).

A strong inverse proportionality of u' with τ_{res} (and the extent of fuel vaporization, F_v) for both global equivalence ratio conditions suggests that the local flow

velocity perturbations are caused by instantaneous droplet evaporation. Instantaneous droplet evaporation induces local flow perturbation though the interaction between Stefan flow and the density difference during the phase change [70, 71]. The time interval of flow from the nozzle exit to the flame surface is estimated as ~ 10 ms for the conditions tested. Based on the extent of fuel vaporization shown in Figs. 3.9(c) and 3.10(c), the resultant change of effective equivalence ratio due to the continuous fuel droplet evaporation between nozzle exit and flame surface is estimated to be < 0.01 for the worst case, suggesting indiscernible variations of effective equivalence ratio. Furthermore, the convective time scale for mixing induced by flow perturbation can be estimated O(1 ms) with u' and the average interval between droplets ($\sim 10d_{30}$) at τ_{res} ~ 0.2, suggesting relatively strong mixing prior the flame surface.

When a small fuel droplet penetrates through the premixed flame preheat zone, it might be immediately vaporized, thus forming either a locally fuel-rich condition or a diffusion flame. Each phenomenon can result in potential acceleration of flame propagation due to the local mixture fraction gradient [72-74]. To address this possibility, the effective burning area defined by flame surface perimeters were evaluated from 50 images of OH PLIF by varying τ_{res}. Although not shown in the figure, the effective burning area exhibits a monotonically increasing trend with u', but with no apparent relation to d_{30}. Nevertheless, the OH PLIF images in Figs. 3.11(a) and 3.11(c) show locally perturbed flame curvature associated with droplet evaporation and/or formation of diffusion flame. However, the OH LIF intensities along the wrinkled flame surface exhibits indiscernible changes, thus their contributions to the overall burning rate can be assumed to be minimal. Consequently, the vaporized fuel/air mixture can be considered

to be spatially uniform, allowing the evaluation of its laminar flame speed based on the effective equivalence ratio derived from the extent of fuel vaporization.

In the previous studies [75-77], it was reported that the existence of small fuel droplets could trigger the diffusive-thermal instability, thus potentially enhancing flame propagation. While such a flame surface instability was not observed in the partially vaporized conditions for either global equivalence ratio studied, it is found at higher extents of fuel vaporization at $\varphi_g = 1.4$. PLIF images for Mixture 2 at $\tau_{res} = 0.70\ s$ and $\varphi_g = 1.4$ clearly shows the flame surface characteristics typical to diffusive-thermal instability (Fig. 3.11(d)). A similar behavior was also found for Mixture 1 at $\varphi_g = 1.4$ and near-fully vaporized conditions. In the case of a premixed Bunsen flame with gaseous fuel/air mixture, a diffusive-thermal instability typically occurs when the mixture Lewis

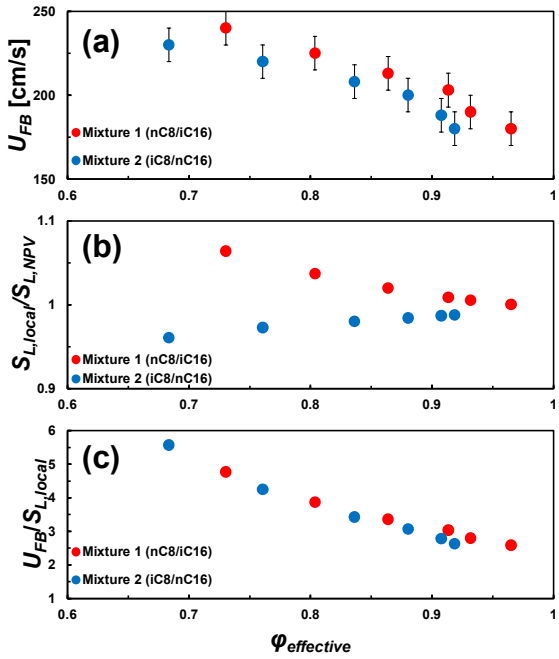

Figure 3.12. Comparison of flashback behaviors two mixtures with $\varphi_{effective}$ at $\varphi_g = 1.0$ in the partially vaporized condition (450 K); (a) the measured U_{FB} values, (b) the ratio of laminar flame speed ($S_{L,local}$) considering the preferential vaporization to the one ($S_{L,NPV}$) without considering the preferential vaporization, (c) the measured U_{FB} values normalized by local laminar flame speed ($S_{L,local}$).

number (Le) is less than unity [78]. Considering the effective Le number (Le) for both mixtures at near-fully vaporized conditions is ~ 1.1, the observed flame surface instabilities could be attributed to the onset of a diffusive-thermal instability due to the existence of small fuel droplets. Further detailed characterization of the instability behavior was not pursued. Rather, the measurements exhibiting instability were excluded in the analysis below so as to focus solely on the evaluating the impact of preferential vaporization on flame flashback behaviors.

Figure 3.12(a) compares the measured U_{FB} values of two mixtures as a function of $\varphi_{effective}$ for measurements performed at $\varphi_g = 1$. The two mixtures should have almost identical laminar flame speed behaviors (thus U_{FB}) as a function of $\varphi_{effective}$ in the absence of preferential vaporization. Thus, the observed difference in U_{FB} must be attributed to the impact of preferential vaporization. The laminar flame speed is a major governing parameter for propagation-driven flashback [43-48]. Therefore, the laminar flame speed ($S_{L,local}$)) with the preferential vaporization and that without ($S_{L,NPV}$) (assuming no change in fuel composition) were calculated using a reduced chemical kinetic model [22]. The ratios of $S_{L,local}$ to $S_{L,NPV}$ as a function of the given $\varphi_{effective}$ are plotted in Fig. 3.12(b). The data shows a disparity between the two mixtures for partially vaporized (low $\varphi_{effective}$) conditions, which essentially disappears as fully vaporized condition ($\varphi_{effective} = \varphi_g = 1$) is approached. Figure 3.12(c) compares U_{FB} normalized by $S_{L,local}$ for the two mixtures, further supporting that the difference in $S_{L,local}$ induced by preferential vaporization primarily governs the observed difference in U_{FB}.

Figure 3.13(a) compares the measured U_{FB} values for the two mixtures as a function of $\varphi_{effective} = \varphi_g = 1.4$. The overall trend of the measured U_{FB} is qualitatively

similar to the results found for $\varphi_g = 1$, i.e., there is a relatively large difference in U_{FB} for partially vaporized conditions that essentially disappears as near-fully vaporized condition are approached, noted by considering $S_{L,local}$ in Fig. 3.13(b). Figure 3.13(c) shows the U_{FB} normalized by $S_{L,local}$, again confirming the significane of preferential vaporization to flame flashback behaviors.

The commonalities in U_{FB} of the two binary component mixtures found through normalization of the data by $S_{L,local}$ for both φ_g conditions in Figs. 3.12(c) and 3.13(c) indicate that preferential vaporization affects global burning characteristic, and hence, flame flashback behavior. Figure 3.14(a) combines the results for both φ_g conditions as a function of $\varphi_{effective}$. The result shows that the normalized U_{FB} by $S_{L,local}$ for the fuel-lean conditions is considerably more sensitive to $\varphi_{effective}$ than for fuel-rich conditions,

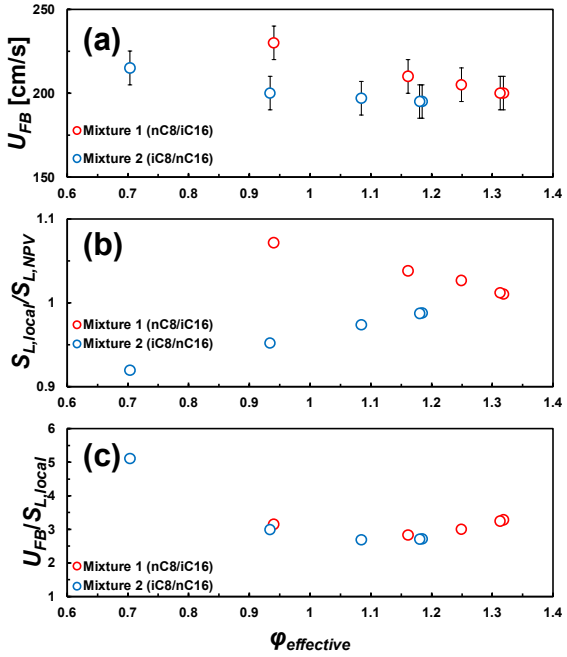

Figure 3.13. Comparison of flashback behaviors two mixtures with $\varphi_{effective}$ at $\varphi_g = 1.4$ in the partially vaporized condition (450 K); (a) the measured U_{FB} values, (b) the ratio of laminar flame speed ($S_{L,local}$) considering the preferential vaporization to the one ($S_{L,NPV}$) without considering the preferential vaporization, (c) the measured U_{FB} values normalized by local laminar flame speed ($S_{L,local}$).

regardless of φ_g. Considering the Reynolds number employed in these measurements based on the nozzle diameter (1000<Re<1600), the premixed Bunsen flames observed here locate in the wrinkled flamelet regime of the Borghi diagram [79, 80]. In these cases, thermo-diffusive effects play an important role in the overall burning rate through interactions with local flow perturbations, thus influencing the local stretch rate [81-85].

As the flames experience flow stretch due to the local fuel evaporation near the flame reaction zone, the overall burning rates are affected by both local laminar flame speed perturbations as well as by flame stretch. The Markstein number, defined as the ratio of Markstein length to flame thickness, characterizes the relative sensitivity of the overall burning rate to the flame surface topology and local flame front curvature. Markstein length (L) can be estimated for a wide range of equivalence ratios as proposed in [84], as well as by considering the effective Lewis number as suggested in [84, 85]. Overall activation energy effects have been evaluated by varying nitrogen dilution of mixtures at the concentration of nitrogen in the mixtures at different equivalence ratios as described in [83].

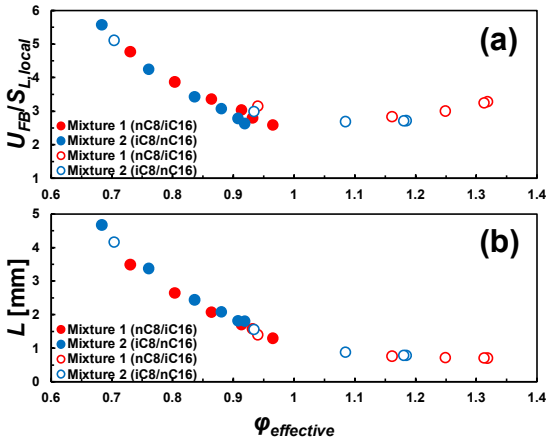

Figure 3.14. (a) Consolidated results of U_{FB} normalized by $S_{L,local}$ for both φ_g conditions, and (b) calculated Markstein length (L) as a function of $\varphi_{effetive}$ in the partially vaporized condition (450 K). Closed symbols are for $\varphi_g = 1.0$ and open symbols are for $\varphi_g = 1.4$.

In the wrinkled flamelet regime, the overall burning rate is affected by the local flow stretch rate (κ) and Markstein length (L) through $S_{overall} = S_L - L\kappa$ [81-85]. Accordingly, the similar tendencies of $U_{FB}/S_{L,local}$ in Fig. 3.14(a) and Markstein length (L) in Fig. 3.14(b) imply that the measured U_{FB} as a function of $\varphi_{effective}$ at fuel-lean conditions is more sensitive to flame stretch caused by local flow velocity perturbations, compared to fuel-rich conditions. Since the premixed Bunsen flame is negatively stretched in general, the higher value of L in lean $\varphi_{effective}$ conditions would make the overall burning rate faster, thus resulting in the increase of $U_{FB}/S_{L,local}$. On the other hand, while the Markstein length monotically decreases with $\varphi_{effective}$, the $U_{FB}/S_{L,local}$ value starts increasing slightly again at $\varphi_{effective} > 1$, which can be attributed to the onset of diffusive-thermal instability as shown in Fig. 3.11(d).

Knowing that the overall burning rate is controlled by the interaction through the local flow stretch rate associated with Markstein length of the partially vaporized fuel/air mixture, Figure 3.15 depicts the normalized U_{FB} by $S_{L,local}$ as a function of ($u'L/S_{L,local}l_f$). Here, the Markstein number (L/l_f) is multiplied to $u'/S_{L,local}$ and the

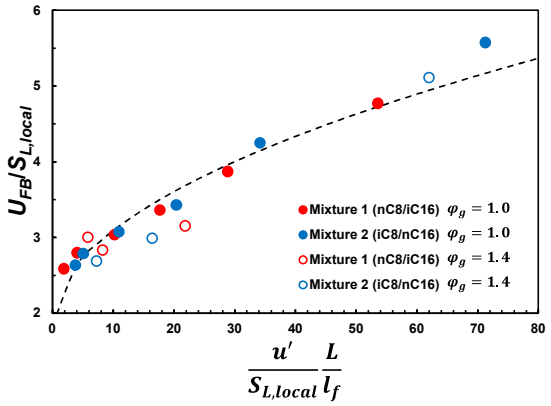

Figure 3.15. Normalized U_{FB} by $S_{L,local}$ as a function of $u'L/S_{L,local}l_f$ in the partially vaporized condition (450 K). Closed symbols are for $\varphi_g = 1.0$ and open symbols are for $\varphi_g = 1.4$.

flame thickness (l_f) is calculated based on the thermal diffusivity and $S_{L,local}$. Following the Damköhler's hypothesis and assuming that $U_{FB}/S_{L,local}$ indicates the overall burning rate at flame flashback, a fitting equation can be derived as Eq. 3.3. Here, measurement points at the near-fully vaporized conditions are excluded from the fitting due to their unique behaviors caused by diffusive-thermal instability.

$$\frac{U_{FB}}{S_{L,local}} = 0.4\left(\frac{u'}{S_{L,local}}\frac{L}{l_f}\right)^{\frac{1}{2}} + 1.85 \qquad \text{(Eq. 3.3)}$$

The derived fitting equation, Eq. 3.3, allows evaluating the relative contributions of laminar flame speed ($S_{L,local}$), local flow velocity perturbation (u'), and preferential vaporization on the observed flame flashback behaviors by incorporating the normalized sensitivity coefficient. Since the local laminar flame speed is directly affected by the extent of fuel vaporization, the relative contribution of $S_{L,local}$ can be regarded as the impact of fuel vapor deposition, defined as $\frac{S_{L,local}}{U_{FB}}\frac{\partial U_{FB}}{\partial S_{L,local}}$. The relative contribution of u' is defined as $\frac{u\prime}{U_{FB}}\frac{\partial U_{FB}}{\partial u}$, which is introduced by the instantaneous fuel droplet vaporization. Finally, the relative contribution of preferential vaporization is determined as $\left|\frac{\eta}{U_{FB}}\frac{\partial U_{FB}}{\partial \eta}\right|$ with $\eta = \frac{S_{L,local}-S_{L,local}}{S_{L,NPV}}$ that compares the difference among the local laminar flame speeds with and without considering the preferential vaporization.

Figure 3.16 compares the relative contributions of laminar flame speed, local flow perturbation, and preferential vaporization at the lowest extents of fuel vaporization of each measurement among two mixtures and two φ_g conditions. The results clearly suggest that the local laminar flame speed plays the most significant role on the flame flashback, since it is directly related with the local fuel vapor deposition. The

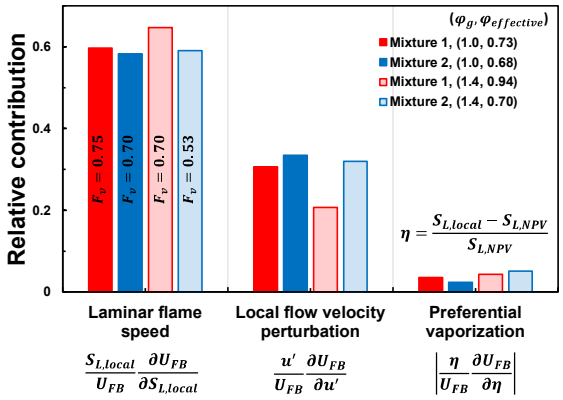

Figure 3.16. Comparison of the relative contributions of laminar flame speed, local flow perturbation, and preferential vaporization based on sensitivity analysis.

contribution from local flow perturbation is found to be secondary in significance, diminishing in importance at the higher extent of fuel vaporization due to the reduced local fuel perturbation at near-fully vaporized conditions.

The contribution from preferential vaporization is found to be relatively weak in comparison, thus of second-order significance under the conditions tested. Its contribution increases with decreasing extent of fuel vaporization and eventually full-vaporized conditions. Nevertheless, note that the impact of preferential vaporization is directly related to changes in local laminar flame speed as a result of the distillation characteristics. Only relatively moderate differences in laminar flame speeds are found for the two n-alkane/iso-alkane mixtures studied here (Figs. 3.12(b) and 3.13(b)) consistent with the noted, relatively weak dependence of flashback behaviors on preferential vaporization. However, the potential significance of preferential vaporization on flame flashback cannot be overlooked for cases such as considering the use of crude oil in gas turbine combustion [86-88]. In such a case, there is a much wider range of boiling temperatures combined with substantial differences in chemical functional group distribution over the distillation curve [89]. The present study evaluates the role of

preferential vaporization on flame flashback behavior primarily governed by laminar flame speed that exhibits only moderate dependency on fuel chemical property (chemical kinetic potential). For other combustion behaviors primarily controlled by flame extinction and/or ignition characteristics, the relative contribution of preferential vaporization could be further magnified due to the pronounced influence from fuel chemical properties.

CHAPTER 4

IMPACT OF PREFERENTIAL VAPORIZATION ON DIFFUSION FLAME EXTINCTION

To establish the envelope of operation condition for turbine engines, it is essential to understand the characteristics of flame extinction. Compared to the extinction behaviors of premixed flames, observing diffusion flame extinction provides the fundamental benefits to understand the coupling effects between chemical reaction and fuel transport. The diffusion flame extinction depends on the heat loss from the flame to surrounding in comparison with the heat release generated during combustion process. To investigate the extinction phenomena of diffusion flame, extensive studies on the flame extinction of diffusion flames have been experimentally and numerically conducted in counterflow configuration, which is widely utilized due to its simple geometry to observe stretched flames [90-97]. In this counterflow configuration, flow strain rate affects the flames by controlling the time scales of mass transport and chemical reaction, characterized as Damkhöler number (D_a) defined by the ratio of mass transport time scale to chemical reaction time scale. Diffusion flame extinction can be clearly examined by the radical index of fuel molecule and transport weighted enthalpy, which is the combination of fuel concentration, heat of combustion, and molecular weight [54, 98].

The objective of this study is to investigate the impact of preferential vaporization of multi-component liquid fuel on diffusion flame extinction in counterflow

configuration. A counterflow burner has been developed including an adjustable vaporization section to control the extent of fuel vaporization. Various n- and iso-alkane liquid fuels were tested first to measure the extinction strain rate of diffusion flame when fully vaporized at 450 K. Three binary mixtures were prepared to have identical transport weighted enthalpy combined with radical index but showing different vaporization characteristics. Then, the extinction strain rate was measured for the two mixtures at fully vaporized condition. To observe the impact of preferential vaporization, the strain rate at diffusion flame extinction was measured by controlling the extent of fuel vaporization at 450 K. In order to evaluate the impact of preferential vaporization, fuel droplet size and velocity were measured by utilizing Phase Doppler Particle Analyzer (PDPA).

4.1 Experimental methodology

4.1.1 Experimental apparatus

Figure 4.1 shows the experimental apparatus including the counterflow burner together with the vaporization section for liquid fuel evaporation. This burner comprises upper and lower parts having 20 mm of inner diameter and 34 mm of outer diameter at the exit with 15 mm of separation distance between the exits. The upper part is a part of typical counterflow burner, having uniform flow velocity profile at the exit through stainless steel mesh and ceramic honeycomb. On the other hand, the lower part has the vaporization section for the liquid fuel evaporation including a liquid fuel injector for making fuel spray. This part was developed by modifying the spray burner used in previous chapter. To achieve uniform flow velocity at the exit, a converging section reducing the diameter from 50 mm to 20 mm with 75 mm in length is located with a outer nozzle to introduce shroud nitrogen. The flow uniformity and spray characteristics as

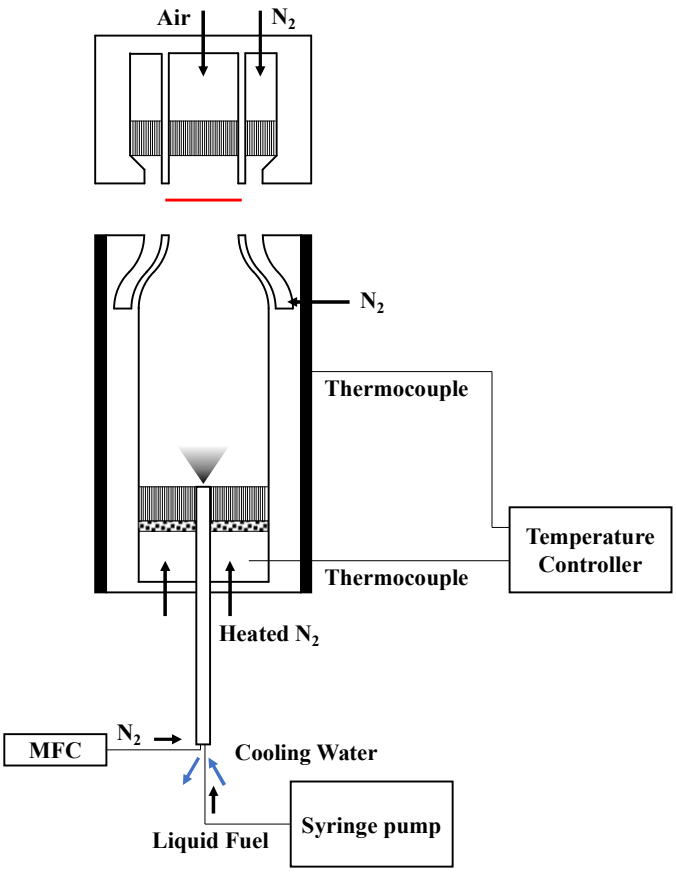

Figure 4.1. Schematics of counterflow burner combined with spray burner.

well as how to estimate the extent of fuel vaporization from the spray burner is explained in previous chapter in detail.

Air as an oxidizer was transported at 300 K through the inner nozzle of upper part, while fuel and nitrogen were supplied at 450 K through the inner nozzle of lower part. Additional nitrogen flows were introduced through the outer nozzles of upper and lower parts to suppress the disturbances from surrounding to the flame. The flow rates of nitrogen and air were regulated by sonic nozzles and mass flow controller, which were calibrated with DryCal 800 (Mesa Labs) at room temperature. Liquid fuel is delivered by a high-pressure syringe pump (Harvard Apparatus, PHD 2000). Then, the volumetric flow rate is defined as the sum of fully vaporized fuel and nitrogen flow rates. During the

experiment, flame extinction behaviors were investigated by controlling global strain rate (a) defined as,

$$a = \frac{2V_O}{L}\left(1 + \frac{V_F}{V_O}\sqrt{\frac{\rho_F}{\rho_O}}\right) \qquad \text{(Eq. 4.1)}$$

where V and ρ are the flow velocity at the nozzle exit and the density, respectively. Here, subscripts F and O denote fuel and oxidizer. L represents the separation distance between two exits.

4.1.2 Formulation of binary component test mixtures

Transport weighted enthalpy (TWE) is the concept including fuel mass diffusion and potential enthalpy produced during the oxidation process of fuel [98]. It is defined as $[Fuel]\Delta H_C\left(MW_{N_2}/MW_{Fuel}\right)^{0.5}$. Here, $[Fuel]$ and ΔH_C are the concentration and heat of combustion of fuel molecule. MW represents the molecular weight. The subscriptions N_2 and $Fuel$ represent nitrogen and fuel at fuel side. By introducing radical index (Ri), which represents relative amount of OH radical in flame reaction zone, it is found that the extinction strain rate of diffusion flame is well characterized [98]. To calculate Ri, which is defined as $Ri = \zeta_{OH,fuel}/\zeta_{OH,n-alkane}$ where $\zeta_{OH} = [OH]_{max} \times \frac{\delta_{OH}}{L} \times a$, the strain rate at diffusion flame extinction was calculated using Chemkin with reduced chemical

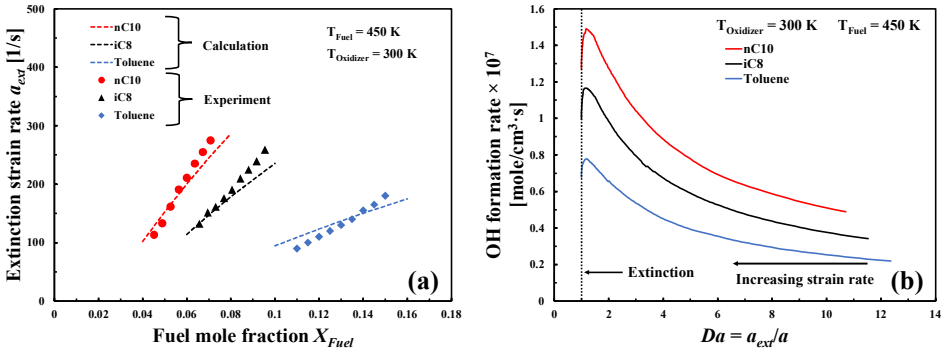

Figure 4.2. (a) Calculated and experimental strain rate as a function of fuel mole fraction at diffusion flame extinction and (b) global OH formation rate as a function of D_a for iC8, nC10, and toluene.

Table 4.1. Summary of properties for components used in this study.

Fuel	MW [g/mol]	ΔH_C [kJ/mol]	Ri
nC8	114.23	5116	1
nC10	142.29	6345	1
nC12	170.33	7347	1
nC16	226.41	10033	1
iC8	114.23	5102	0.77
iC16	226.41	10002	0.77
Toluene	92.14	3771	0.51

kinetic models for n-decane (nC10), iso-octane (iC8) and toluene. Here, $[OH]_{max}$ and δ_{OH} are the peak OH concentration and thickness, respectively.

Figure 4.2(a) shows calculated extinction strain rate for nC10, iC8, and toluene with experimental results. It shows that the behavior of calculated extinction strain rate through the reduced chemistry models are well agree with that of experimental results. Figure 4.2(b) shows the global formation rate of OH in the flame reaction zone as a function of D_a. The volumetric OH production rate is enhanced as the flow strain rate increases until D_a becomes around 1.5. In this regime, the time scale of chemical reaction in the flame reaction zone is very short compared to that of mass transport into the flame. However, as the strain rate further increases, the thermal diffusion layer by high temperature of the flame becomes thinner due to the convective momentum, leading to

Table 4.2. Summary of component and properties for binary mixtures used in this study.

	Mixture 1	Mixture 2	Mixture 3
nC8	0.5		
nC12			0.89
nC16		0.5	
iC8		0.5	
iC16	0.5		
Toluene			0.11
Ri	0.88	0.88	0.94
ΔH_C [kJ/mol]	7559	7568	6954
MW [g/mol]	170.32	170.32	161.73

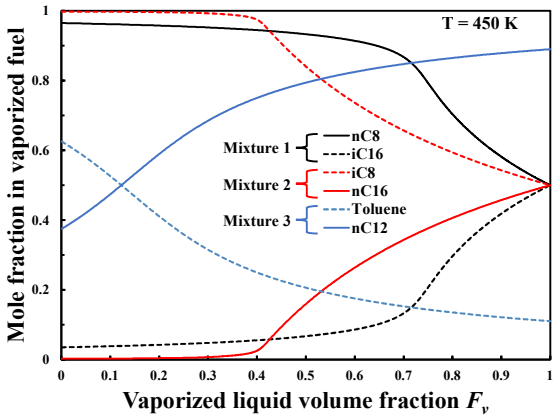

Figure 4.3. Mole fraction in vaporized fuel as a function of vaporized liquid volume fraction for binary mixtures at 450 K.

the decrease in the flame temperature through the heat loss. Further increase of strain rate enhances the heat loss. Then, excessive heat loss extinguishes the flame by the decreased OH formation rate due to the lowered flame temperature. As defined, Ri can be found from the Fig. 4.2(b). Table 4.1 shows the summary of properties including Ri, ΔH_C, and MW for several components (n-octane (nC8), n-decane (nC10), n-dodecane (nC12), n-hexadecane (nC16), iso-octane (iC8), iso-cetane (iC16), toluene) used in this study.

To investigate the impact of preferential vaporization, three different binary mixtures were formulated by matching $Ri \times TWE$ at fully vaporized condition but having different vaporization characteristics. Table 4.2 shows the composition and properties of mixtures. Those mixtures consist of different components that have different physical and chemical properties. Therefore, the mixtures will exhibit different vaporization behavior. Figure 4.3 shows the mole fraction of vaporized components as a function of vaporized liquid volume fraction calculated by vapor pressure of each component in the mixture. It shows that lighter components (e.g., nC8, iC8, and toluene) evaporate earlier than heavier components (e.g., iC16, nC16, and nC12) due to the difference in the vapor pressure between the lighter and heavier components. This indicates that the behavior of diffusion

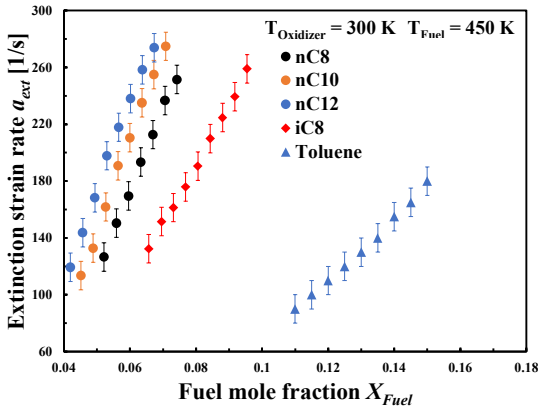

Figure 4.4. Strain rate at diffusion flame extinction as a function of fuel mole fraction for several pure components, n-octane (nC8), n-decane (nC10), n-dodecane (nC12), iso-octane (iC8), and toluene at fully vaporized condition.

flame extinction will be influenced by the change of composition of vaporized component.

4.2 Diffusion flame extinction at fully vaporized condition

The extinction of diffusion flame for fully vaporized condition was first observed to understand how it behaves depending on the fuels before the impact of preferential vaporization on the diffusion flame extinction is investigated. Figure 4.4 shows the strain rate at diffusion flame extinction as a function of fuel mole fraction for nC8, nC10, nC12, iC8, and toluene at fully vaporized condition. Here, the extinction strain rate for nC16 and iC16 was not measured due to severe condensation inside the spray burner. Diffusion flame of nC12 exhibits the highest extinction strain rate at same fuel mole fraction. The extinction strain rate becomes lower as the molecular weight of fuel decreases for n-alkanes. Also, the extinction strain rate for nC8 is higher than that of iC8. Toluene exhibits the lowest extinction strain rate in Fig. 4.4. This result is consistent with the expectation based on solely the chemical reactivity potential (e.g., DCN value) of each fuel. On the other hand, considering that diffusion flame is extinguished by imbalance of

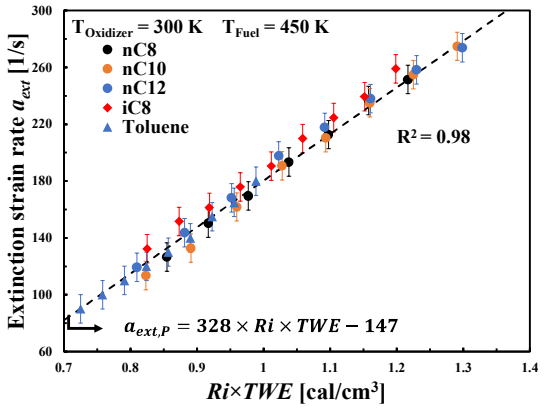

Figure 4.5. Strain rate at diffusion flame extinction as a function of $Ri \times TWE$ for several pure components, n-octane (nC8), n-decane (nC10), n-dodecane (nC12), iso-octane (iC8), and toluene at fully vaporized condition.

heat and fuel mass diffusions near flame reaction zone, fuel mole fraction is not enough to examine the diffusion flame extinction.

Considering that Ri and TWE represent the chemical kinetic potential and the potential enthalpy weighted by mass transport through diffusion process, respectively, the extinction strain rate of fully vaporized single component fuels can be characterized by $Ri \times TWE$ as shown in [98]. Figure 4.5 shows the extinction strain rate as a function of $Ri \times TWE$ for the single component fuels. The extinction strain rate is well characterized by the value of $Ri \times TWE$, which indicates that the concept of TWE weighted by Ri is proper parameter to explain the behavior of diffusion flame extinction. The correlation equation between $Ri \times TWE$ and a_{ext} is found.

$$a_{ext,P} = 328 \times Ri \times TWE - 147\ [s^{-1}] \qquad \text{(Eq. 4.2)}$$

For the mixtures shown in Table 4.2, the extinction strain rate was measured at fully vaporized condition. As the three binary mixtures were formulated to share same $Ri \times TWE$ for the identical extinction behavior of diffusion flames when fully vaporized, the behavior of extinction strain rate at fully vaporized condition was investigated to

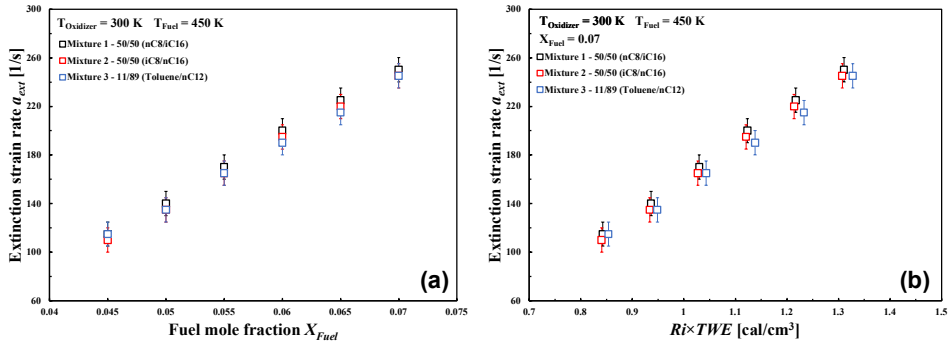

Figure 4.6. Strain rate at diffusion flame extinction as a function of (a) fuel mole fraction and (b) $Ri{\times}TWE$ for three binary mixtures at fully vaporized condition.

verify the correlation between the extinction strain rate and $Ri \times TWE$. Figure 4.6(a) and (b) shows the extinction strain rate as a function of fuel mole fraction and $Ri \times TWE$. Three binary mixtures exhibit identical behavior of diffusion flame extinction in terms of both mole fraction and $Ri \times TWE$. This result confirms that the fuels that have the same $Ri \times TWE$ exhibit the identical extinction behavior.

4.3 Diffusion flame extinction at partially vaporized condition

To investigate the impact of preferential vaporization on the diffusion flame extinction, the strain rate at the flame extinction was measured for the three binary mixtures by changing the location of spray injector. Figure 4.7(a) shows the extinction strain rate as a function of injector location at 0.07 of global fuel mole fraction $X_g = 0.07$ for the three mixtures and nC8. The injector location is defined as the distance from the nozzle exit to the spray injector. At longer injector location, the three mixtures exhibit almost identical extinction strain rate due to fully vaporized fuels. However, as the injector location moves to the nozzle exit, the tendency of extinction strain rate exhibit different behaviors, showing the larger difference in the extinction strain rate at shorter injector location. When the flame is extinguished with full vaporized fuels at longer injector location, it is flat in flame surface. However, at shorter injector locations, the

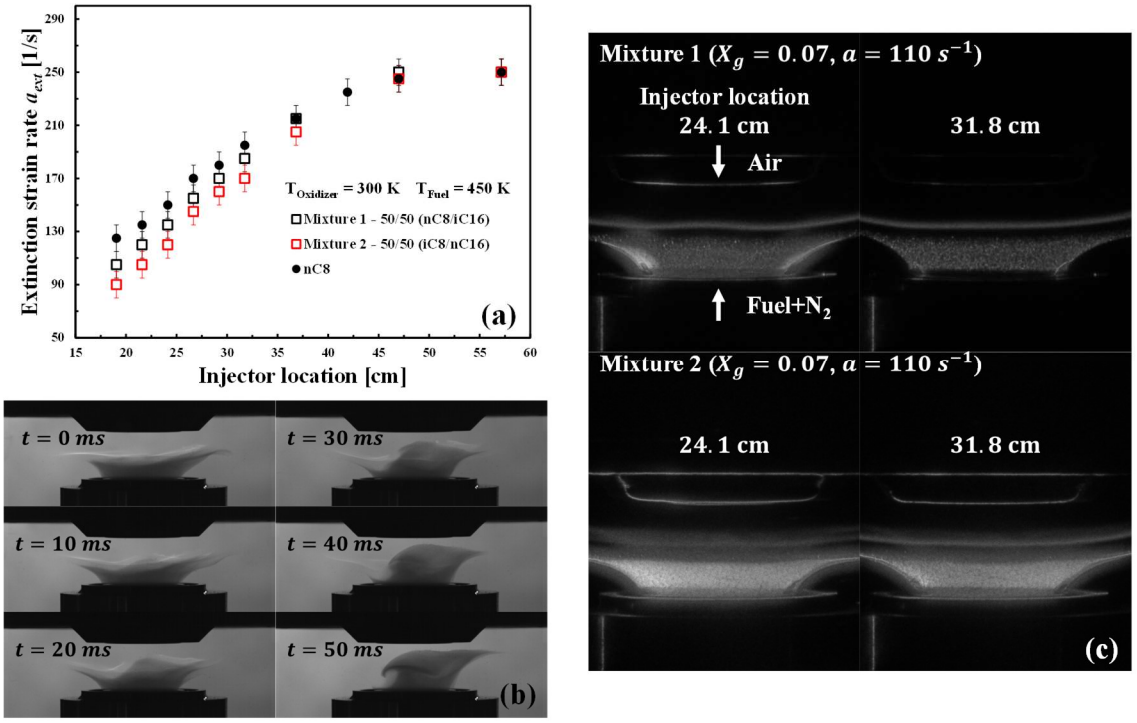

Figure 4.7. (a) Extinction strain rate as a function of injector location at $X_g = 0.07$ for binary mixtures and at $X_g = 0.076$ for nC8, (b) sequential images of diffusion flame extinction of mixture 2 at injector location of 19 cm, $X_g = 0.07$, and $a = 100\ s^{-1}$, and (c) OH PLIF images at different injector locations for binary mixtures at $X_g = 0.07$ and $a = 110\ s^{-1}$.

flame surface is more perturbed by local fuel evaporation and spray dynamics as previously discussed in chapter 3. This flow perturbation causes the complicated behavior of diffusion flame extinction. Figure 4.7(b) shows the sequential images with relative time during the diffusion flame extinction for mixture 2. Locally perturbed stream with partially vaporized fuel pushes the flame to oxidizer side. Then, it makes a hole at $t = 20\ ms$, resulting in the complete diffusion flame extinction at $t = 50\ ms$.

The extinction of diffusion flame is sensitive to not only $Ri \times TWE$ but also flow fluctuation. Figure 4.7(c) shows OH PLIF images for the Mixture 1 and 2 at different flow residence times. Detailed information about OH PLID is mentioned in the chapter 3. Two parts are shown in the figures. The straight line in the middle represents the OH

signal from the flames, while broad intensity signal coming from Mie scattering on fuel side shows fuel spray. At shorter injector location, the intensity coming from the fuel spray becomes stronger due to larger number density of fuel droplets in the spray, meaning that the liquid fuel is less vaporized at the burner exit. As the fuel spray reaches the flame reaction zone, most of fuel droplets are vaporized in thermal boundary layer. The intensity between the flame and fuel spray confirms fuel vaporization near the flame, meaning that the potential enthalpy provided into the flame, which is represented as TWE, is identical for the Mixture 1 and 2. Even, at the injector location at 24.1 cm (near extinction condition), the intensity between the flame and spray is still found, meaning that most of fuel droplets is vaporized. However, preferential vaporization will still influence the diffusion flame extinction through the variation of Ri in thermal diffusion layer and/or flame reaction zone during the fuel evaporation.

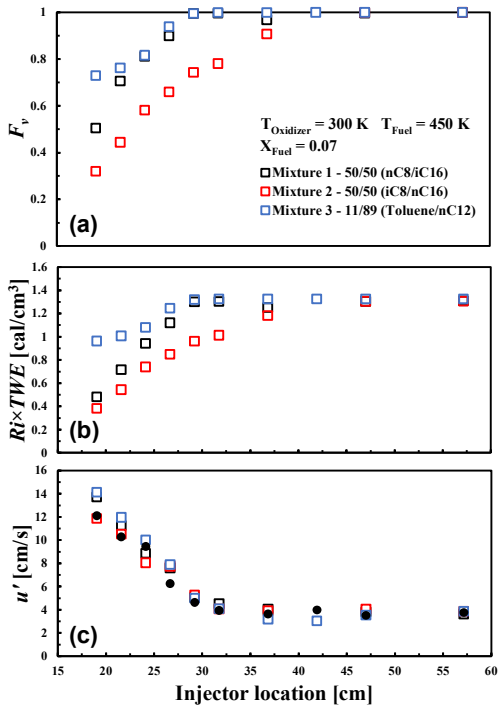

Figure 4.8. (a) Extent of fuel evaporation, (b) $Ri \times TWE$, and (c) flow fluctuation as a function of injector location at flame extinction for the mixtures and nC8.

To understand the behavior of diffusion flame extinction in detail, the spray properties such as droplet size and flow fluctuation were measure by PDPA as shown in chapter 3. Based on the PDPA data, the extent of fuel evaporation (F_v) and the composition of fuel vapor at the nozzle exit was also calculated to estimate the values of Ri and TWE. Figure 4.8(a) shows the extent of fuel evaporation at the nozzle exit as a function of injector location when the flame is extinguished. At longer injector location (> 40 cm), the three mixtures are fully vaporized, showing the identical extinction strain rate in Fig 4.7(a). However, the mixtures become partially vaporized at shorter injector locations. At fixed location, Mixture 2 is less vaporized than others, while Mixture 3 is more vaporized than others. This difference in the extent of fuel evaporation is caused by the vapor pressures of components in the mixtures. nC16 in Mixture 2 has the lowest vapor pressure among the heavier ends of mixtures, while nC12 in Mixture 3 has highest vapor pressure. This characteristic of evaporation behavior causes the change in the components of vaporized fuel as shown in Fig. 4.3. The difference in the fuel evaporation characteristic of mixtures causes the variation of vaporized fuel composition, leading to different chemical kinetic potential and potential enthalpy as well as mass transport of vaporized fuel. Figure 4.8(b) shows $Ri \times TWE$ calculated from F_v in Fig. 4.8(a) as a function of the injector location for the mixtures and nC8. While $Ri \times TWE$ of nC8 exhibits identical value at every location as nC8 is nearly fully vaporized, $Ri \times TWE$ of mixtures decreases at shorter injector location where the mixtures are partially vaporized. $Ri \times TWE$ of Mixture 2 exhibits lowest value than others due to that of lighter component (iC8) at partially vaporized conditions. $Ri \times TWE$ of Mixture 3 at partially vaporized condition is higher than Mixture 1 and 2 due to the vaporized nC12 in gas

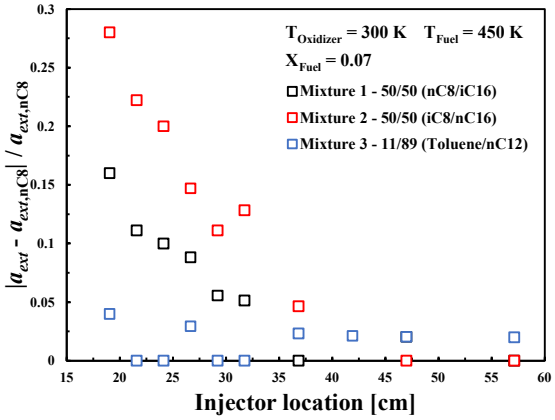

Figure 4.9. Normalized extinction strain rate as a function of injector location at flame extinction for three binary mixtures.

phase fuel. The result of $Ri \times TWE$ for the mixtures indicates that the extinction strain rate behavior shown in Fig. 4.7(a) is determined by $Ri \times TWE$ considering the impact of preferential vaporization.

At shorter injector location, the flow field is perturbed by local flow evaporation of liquid fuel and spray dynamics as shown in Fig. 4.7(b). When the flow stream is fluctuating, the strain rate will be locally enhanced by flow fluctuation. With eddy motion generated by flow fluctuation, turbulence can create additional diffusion process and flow stretch rate. Even though the turbulence energy by small eddies is weaker than that by large eddies, local flow stretch through the small eddies is stronger than that through the large eddies due to abrupt change in flow velocity. Then, the extinction of diffusion flame can be achieved at lower strain rate [99-102]. Figure 4.8(c) shows the flow fluctuation as a function of injector location at the diffusion flame extinction for the mixtures and nC8. The behavior of flow fluctuation for the mixtures is identical, meaning that its impact on the extinction strain rate of diffusion flame would be similar.

While nC8 is almost fully vaporized at every injector location in this study, the flow fluctuation of nC8 exhibits similar tendency, meaning that the change in the

extinction strain rate for nC8 shown in Fig. 4.7(a) indicates the influence of flow fluctuation. Therefore, in order to evaluate the relative contribution of preferential vaporization impact on diffusion flame extinction, the extinction strain rate of mixtures is normalized with that of nC8. The normalized extinction strain rate defined as $\frac{|a_{ext}-a_{ext,nC8}|}{a_{ext,nC}}$ is shown in Fig. 4.9 at different injector locations. As the impact of preferential vaporization does not exist for nC8, the normalized extinction strain rate solely represents the impact of preferential vaporization. At longer injector location, three mixtures are nearly fully vaporized, exhibiting very small values for the normalized extinction strain rate. However, at partially vaporized conditions, the normalized extinction strain rate becomes larger as the injector location is closer to the burner exit. This indicates that the preferential vaporization influences the behavior of diffusion flame extinction.

To further investigate the impact of preferential vaporization in large fuel mole fraction, the extinction strain rate is measured for different global fuel mole fractions at the fixed injector location of 26.7 cm. Figure 4.10(a) shows the extinction strain rate as a function of global fuel mole fraction (X_g) for the Mixture 1 and 2. The dashed line represents the extinction strain rate predicted by the correlation equation between

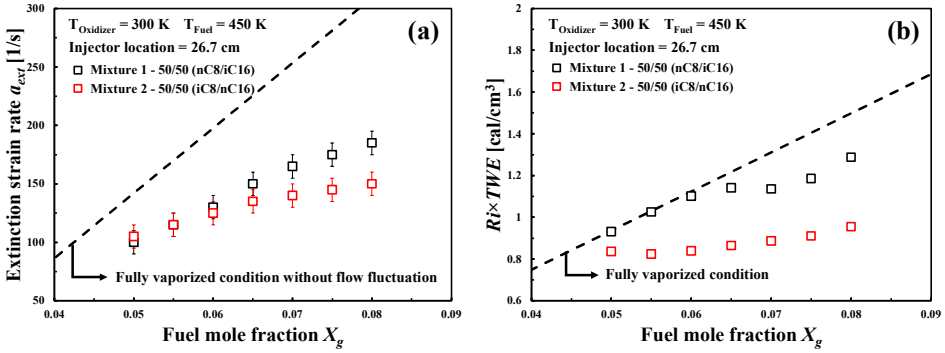

Figure 4.10. (a) Extinction strain rate and (b) $Ri \times TWE$ as a function of fuel mole fraction for binary mixtures at injector location of 26.7 cm.

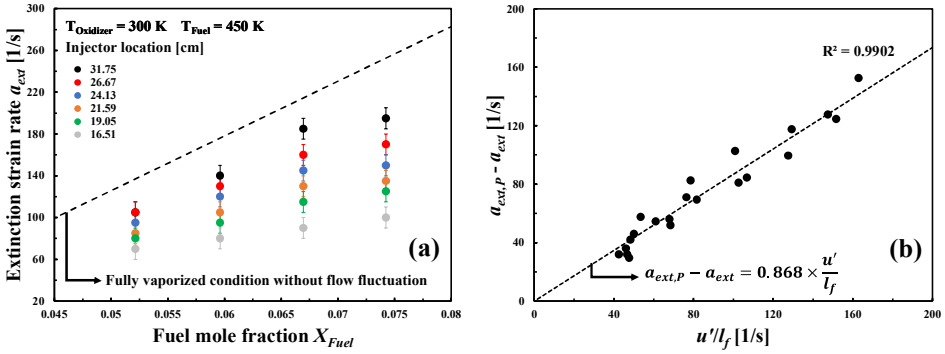

Figure 4.11. (a) Extinction strain rate of nC8 as a function of fuel mole fraction for several injector locations at fully vaporized condition and (b) $a_{ext,P} - a_{ext}$ as a function of u'/l_f.

$Ri \times TWE$ and a_{ext} shown in Fig. 4.5. The discrepancy between the measured and predicted extinction strain rates is due to the flow fluctuation and preferential vaporization. Figure 10(b) shows $Ri \times TWE$ at the flame extinction though the PDPA measurement as a function of global fuel mole fraction for the Mixture 1 and 2. Mixture 1 is fully vaporized until $X_g = 0.65$, while Mixture 2 is near fully vaporized at $X_g = 0.05$, meaning that the impact of preferential vaporization will appear as much as the difference in $Ri \times TWE$ between the mixtures and prediction.

The extinction strain rate of fully vaporized nC8 is measured to evaluate the impact of flow fluctuation. Figure 4.11(a) shows the extinction strain rate as a function of X_g at different injector locations with predicted extinction strain rate calculated from the correlation equation. It clearly shows the impact of flow fluctuation through the difference in extinction strain rate between the measured and predicted extinction strain rate. The flow stretch induced by flow fluctuation lowers the extinction strain rate as much as its contribution. This can be scaled by u' and flame thickness (l_f), which is estimated by $(\alpha/a_{ext})^{\frac{1}{2}}$. Here, α is thermal diffusivity. Figure 4.11(b) shows the difference between measured and predicted extinction strain rates ($a_{ext,P} - a_{ext}$) as a

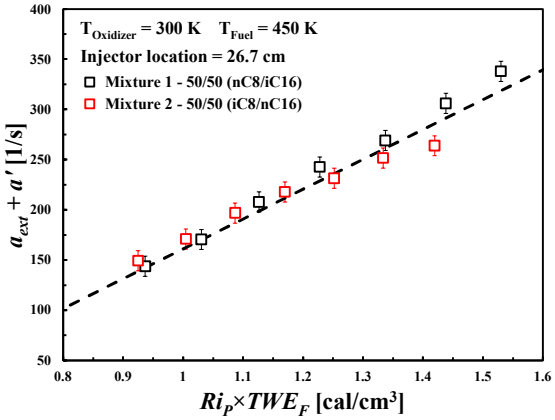

Figure 4.12. $a_{ext} + a'$ as a function of $Ri_P \times TWE_F$ for binary mixtures at injector location of 26.7 cm.

function of u'/l_f. It is found that $a_{ext,P} - a_{ext}$ and u'/l_f exhibit linear relationship with R^2 value of 0.99. Therefore, the flow stretch induced by flow fluctuation (a') can be estimated.

$$a' = a_{ext,P} - a_{ext} = 0.868 \times \frac{u'}{l_f} \qquad \text{(Eq. 4.3)}$$

As shown in Fig. 4.7(c), the fuel droplets are near fully vaporized, meaning that the potential enthalpy provided into the flame is identical for the Mixture 1 and 2. However, the preferential vaporization will still appear due to the fuel evaporation in the thermal diffusion layer and/or flame reaction zone. In this regard, $a_{ext} + a'$ is calculated as a function of $Ri_P \times TWE_F$ in Fig. 4.12. Here, the subscripts P and F represent the partially and fully vaporized conditions. The dashed line shows the predicted extinction strain rate at fully vaporized condition without the flow fluctuation. This indicates that the extinction strain rate including the impacts of flow fluctuation and preferential vaporization is successfully characterized.

To evaluate the contribution of flow fluctuation and preferential vaporization to the extinction strain rate, the feature sensitivity analysis has been done. The relative

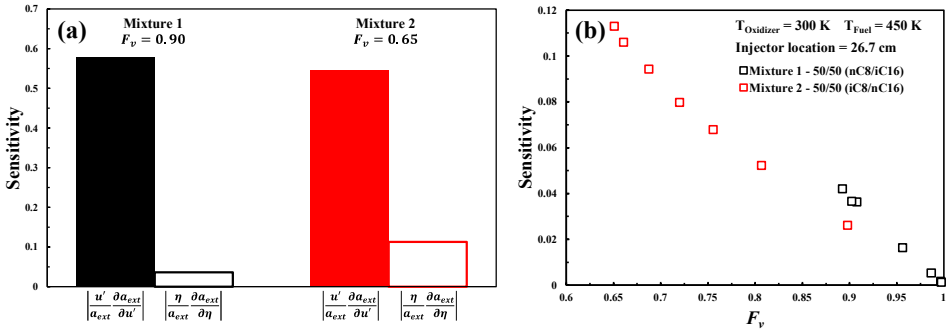

Figure 4.13. (a) Sensitivities of flow fluctuation and preferential vaporization and (b) sensitivity of preferential vaporization as a function of vaporized liquid volume fraction for binary mixtures at injector location of 26.7 cm.

contribution of u' can be defined as $\left|\frac{u'}{a_{ext}}\frac{\partial a_{ext}}{\partial u'}\right|$. The relative contribution of preferential vaporization is defined as $\left|\frac{\eta}{a_{ext}}\frac{\partial a_{ext}}{\partial \eta}\right|$ with $\eta = \frac{Ri_F - Ri_P}{Ri_F}$ that compares the difference in the radical index between fully and partially vaporized conditions. Figure 4.13(a) shows the sensitivities of u' and η for the Mixture 1 and 2 at the lowest F_v in this study. Compared to the flow fluctuation, the preferential vaporization is relatively weak to the extinction strain rate, thus of second order in this study. Nevertheless, Fig. 4.13(b) shows that the contribution of preferential vaporization to the extinction strain rate becomes important when the extent of fuel vaporization decreases.

CHAPTER 5

INTERACTION OF DIFFUSION/PREMIXED FLAMES WITH ISOLATED SINGLE DROPLET

In chapter 3 and 4, the impact of preferential vaporization on flame flashback and extinction of diffusion flame had been discussed. Even though flow fluctuation induced by locally vaporizing fuel droplets and spray dynamics influenced the flame flashback and the extinction of diffusion flame, partially vaporized fuel spray could affect the combustion behaviors through the preferential vaporization. In case of the extinction of diffusion flame discussed in chapter 4, most of fuel droplets are vaporized due to the small size of droplet and the residence time in the thermal diffusion layer. On the other hand, as discussed in chapter 3, some fuel droplets big enough could penetrate the flame reaction zone with short residence time, resulting in the flow perturbation through the fuel vaporization near the flame reaction zone. Such a complex interaction between the fuel spray and flame makes it difficult to understand and evaluate the impact of preferential vaporization on the combustion behaviors.

The extinction of premixed and diffusion flames is governed by the heat release produced during oxidation process and the heat loss from the flame to surrounding. Extensity studies have shown that the premixed/diffusion flame extinction can be achieved by flame stretch, radiation heat loss, and Lewis number [90-97, 103-109]. Compared to typical flames with gaseous fuel, when the fuel droplet is on the flames,

heat absorbed by the fuel droplet lowers the local flame temperature around the droplet, leading to thermal quenching. Then, vaporized fuel and its amount determines broader or narrower flame extinction limit by enhancing or weakening the chemical reaction in flame reaction zone. Moreover, the fuel droplet penetrating through the flame perturbs flame structure by fluctuating flow field. Therefore, the size and the residence time of fuel droplet near the flame are important factors in terms of heat absorption from the flames determining the flame extinction limit.

To fundamentally understand the impact of preferential vaporization interacting with flames, it is necessary to investigate the interaction between single droplet of multi-component liquid fuel and the flame. Extensive studies have been conducted to understand the vaporization of liquid fuel droplet for single and multi-component liquid fuels [110-114]. Recent study has highlighted that the preferential vaporization of multi-component fuel droplets plays a significant role on determining the combustion behaviors at larger size of fuel droplets [115]. Especially, the evaporation of fuel droplets near the flame reaction zone affects local fuel mole fraction as well as flow dynamics around the fuel droplets. Therefore, it is required to observe solely preferential vaporization. In this regard, the interaction between the single fuel droplet of multi-component fuel and the premixed/diffusion flames will be investigated.

In this chapter, the interaction of isolated single droplet with premixed and diffusion flames at near extinction conditions was investigated by utilizing a counterflow burner integrated with a piezo-electric assisted single droplet generator. Either premixed or diffusion flames were formed by using methane/air or methane/nitrogen mixtures at one side of the counterflow burner, while the other side was supplied by either nitrogen

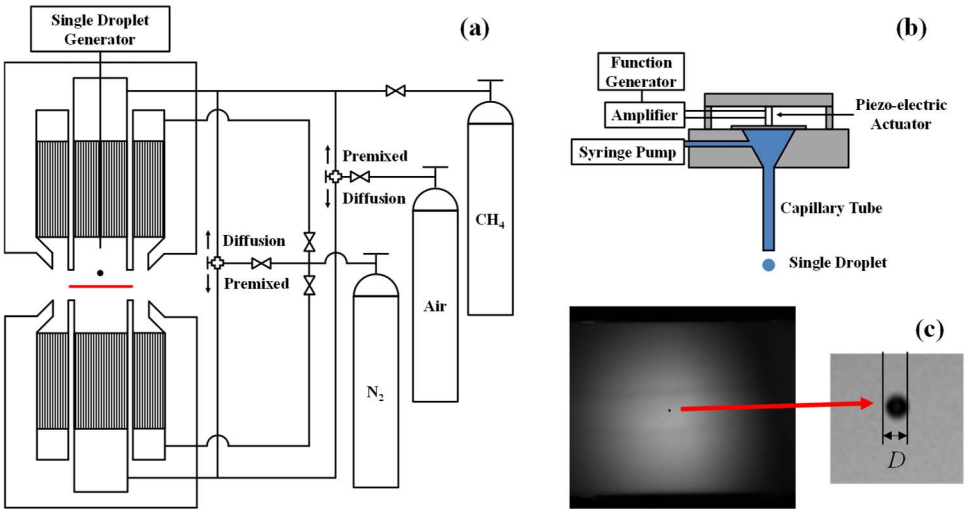

Figure 5.1. (a) Schematic of the counterflow burner, (b) single droplet generator, and (c) direct picture of single droplet.

(for premixed flame) or air (for diffusion flame). Various n-alkane and aromatic liquid fuels were used to generate isolated single droplet, which initial liquid droplet diameter was controlled by piezo-electric pulse.

5.1 Experimental methodology

5.1.1 Experimental apparatus

Figure 5.1(a) shows the experimental apparatus including the counterflow burner together with the piezo-electric single droplet generator. This counterflow burner consists of two identical parts having the inner and outer nozzles, which are 20 mm and 34 mm in diameter, respectively. The separation distance (L) between inner nozzles of both parts is 20 mm. Ceramic honeycombs and stainless steel meshes were installed at 55 mm upstream from the nozzle exits for the uniform flow velocity. Through the inner nozzles, either methane/air or methane/nitrogen mixtures were transported from the one side of the burner in order to establish premixed and diffusion flames, while either nitrogen or air were supplied from the other part of the burner, respectively. Additional nitrogen flows were introduced through the outer nozzles of both upper and lower burners to suppress

disturbances from surrounding to the flame. The flow rates of methane, air and nitrogen were regulated by sonic nozzles, which were calibrated with DryCal 800 (Mesa Labs) at room temperature. During the experiment, flame extinction behaviors were investigated by controlling global strain rate (a) defined as shown in the chapter 4,

$$a = \frac{2V_O}{L}\left(1 + \frac{V_F}{V_O}\sqrt{\frac{\rho_F}{\rho_O}}\right) \qquad \text{(Eq. 5.1)}$$

where V and ρ are the flow velocity at the nozzle exit and the density, respectively. Here, subscripts F and O denote fuel and oxidizer.

To introduce a single liquid fuel droplet on the flame, the piezo-electric droplet generator was developed as shown in Fig 5.1(b). The function generator (Siglent, SDG2042X) produced pulsed signal, which was amplified 20 times through the amplifier (Thorlabs, HVA200) to operate the piezo-electric actuator (Thorlabs, APF503). Then, the piezo-electric actuator generated pressure wave through the liquid fuel in the reservoir by vibrating a thin stainless-steel plate on top of the reservoir, while the liquid fuel was supplied by high-pressure syringe pump (Harvard Apparatus, PHD 2000). A single liquid fuel droplet was injected by the pressure wave at the tip of the capillary tube placed at 50 mm upstream from the inner nozzle of the upper burner. In this study, the liquid fuel droplets were injected from the methane/nitrogen and methane/air mixture sides. For the single droplet injection synchronized with the applied frequency (f), the amplitude of pulsed signal was required to be carefully controlled during the experiment, while the syringe pump supplied the liquid fuels at given flow rate (Q), determining the droplet size (D) of the liquid fuels as $D = \sqrt[3]{\frac{6Q}{\pi f}}$. In this study, various liquid fuels (e.g., n-haptane (nC7), n-dodecane (nC12), n-hexadecane (nC16), iso-octane (iC8), toluene, and 1,3,5

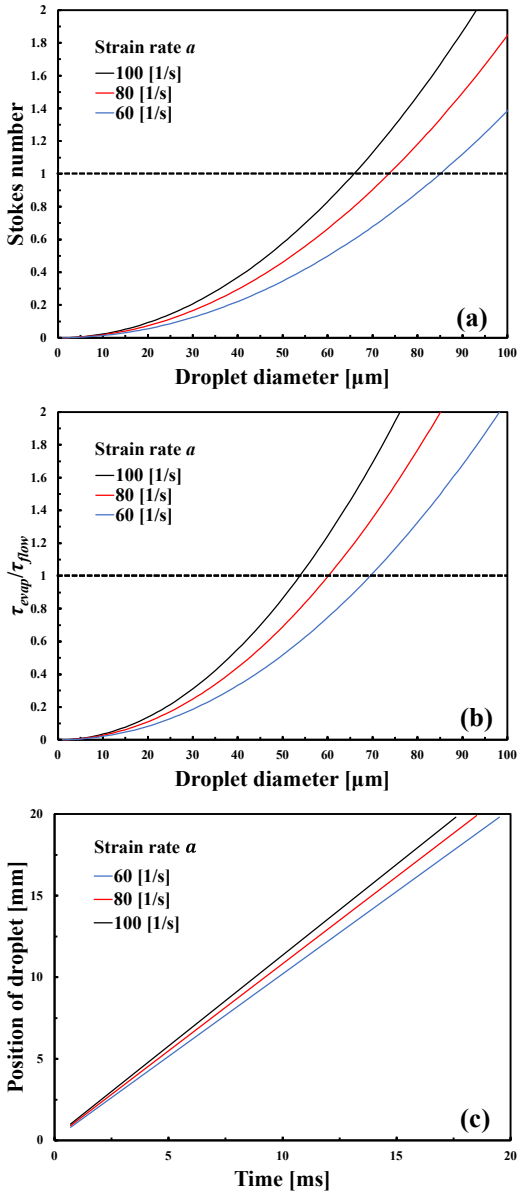

Figure 5.2. (a) Calculated Stokes number and (b) the ratio of evaporation to flow time scales of nC16 droplet as a function of droplet diameter and (c) measured time history of position of droplet for several strain rates.

trimethylbenzene (135 TMB) were used to investigate the impact of preferential vaporization.

5.1.2 Droplet injected through single droplet generator

Single droplet was first analyzed to verify the capability of single droplet generator to create consistent size and velocity. With the source of backlight using LED

(Thorlabs, M530L3) and high-speed camera (Photron, SA-Z), multiple single droplets were captured. Figure 5.1(c) shows the direct picture of single droplet in the middle of counterflow burner. Directly measured sizes from the image were well agree with the size calculated from the equation based on the liquid flow rate and applied frequency within 10 % error.

Droplet velocity in the streamline of surrounding gas flow will differ from the velocity of gas flow due to the momentum of liquid fuel droplet. As shown in the chapter 3, Stokes number (Stk) of single droplet is analyzed to investigate the droplet behavior in counterflow configuration. Figure 5.2(a) shows Stk of n-hexadecane (nC16) droplet as a function of droplet size at different strain rates. In general, it is well known that the droplet follows the flow streamline with 1 % difference in tracing accuracy when Stk is smaller than 0.1. It is found that the droplet size should be between 21 to 27 μm to achieve Stk smaller than 0.1 for the strain rate from 60 to 100 s^{-1}. When Stk is bigger than 0.1, the droplet trajectory deviates from the flow streamline. In this study, the minimum droplet size is 200 μm, meaning that the droplet behavior in counterflow configuration does not follow flow streamline due to high Stk. Figure 5.2(c) shows the time history of position of single nC7 droplet at different strain rates by using the high-speed camera. Even though the flow velocity of gas changes along the centerline with showing zero velocity at the middle, the position of single droplet linearly varies in the increase of time, meaning that droplet velocity is not influenced by the flow velocity of surrounding gas. The velocity of single droplet calculated from Fig. 5.2(b) is order of 1 m/s, while the droplet velocity increases with the strain rate. Considering that the single droplet is injected at 50 mm above the burner exit of upper part, the free fall velocity of

single droplet is order of 1 m/s. This indicates that the droplet behavior is affected by only the gravity, meaning that the residence time of single droplet near the flame is only governed by the flame thickness. Not only that, fuel droplet will take longer time to be vaporized near the flame reaction zone. Figure 5.2(b) shows the ratio of evaporation to flow time scales as a function of droplet diameter. Here, the time scales of fuel evaporation (τ_{evap}) and flow (τ_{flow}) are defined as $\frac{d^2}{K}$ and $\frac{1}{a}$, respectively. d and K represent droplet diameter and evaporation constant. The ratio of time scales of evaporation to flow substantially increases as the droplet size becomes bigger. Therefore, considering the minimum droplet size created in this study, the time scale of droplet evaporation is much longer than that of flow, meaning that the interaction between droplet and flames will be influenced by the initial mole fraction of liquid fuel droplet.

5.2 Interaction between isolated single droplet and diffusion flame

Figure 5.3 shows the extinction strain rate of methane/air diffusion flame as a function of methane mole fraction (X_{CH4}) for various single-component liquid fuels at two different droplet sizes. At 0.46 mm droplet diameter as shown in Fig. 5.3(a), it is found that there is no difference in the extinction strain rate. Compared to the evaporation time of nC7 (~1 s), which is the most volatile component used in this study, the flow

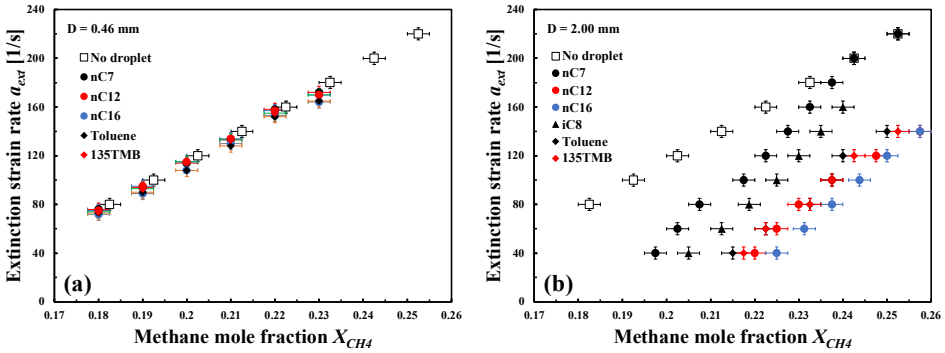

Figure 5.3. Extinction stain rate as a function of methane mole fraction for n-alkanes (nC7, nC12, and nC16), iC8, and aromatics (toluene and 135TMB) at droplet sizes of (a) 0.46 and (b) 2.00 mm.

Table 5.1. Summary P_{vap} of and $Ri \times TWE$ at P_{vap} for single-component fuels used in this study.

Fuel	P_{vap} at 300 K [Pa]	$Ri \times TWE$ [cal/cm^3]
nC7	5330	866.94
nC12	20	4.09
nC16	0.4	0.096
iC8	5500	747.78
Toluene	3088	208.33
135 TMB	320	18.47

residence time of fuel droplet in the flame reaction zone (~1 ms) is too short, meaning that the extent of fuel vaporization is small. Even, the heat loss from the flame to the droplet becomes small due to the small size of fuel droplet. On the other hand, the extinction strain rate shows different tendency for various single-component fuels at the droplet size of 2.00 mm as shown in Fig. 5.3(b). When the fuel droplet penetrates the flame reaction zone, it perturbs the flow field near the flame, which extinguishes the flame due to local flow stretch induced by the droplet. For n-alkanes, the extinction strain rate extends to lower methane mole fraction as the molecular weight of liquid fuel decreases, even though heavier n-alkane molecule provides more enthalpy to sustain the flame. Even, nC12 and 1,3,5 trimethylbenzene (135 TMB) exhibit similar tendency in the extinction strain rate. It is noted that 135 TMB is more volatile than nC12, while the extinction strain rate of 135 TMB is lower than that of nC12 at fully vaporized condition. This implies that not only the chemical kinetic potential but also the vapor pressure determines the extinction behavior of diffusion flame, even though the extent of fuel vaporization is small.

While the droplet penetrates through the flame, small amount of fuel is vaporized on the droplet surface during the short residence time. Therefore, the composition of

vaporized fuel can be estimated from the vapor pressure of liquid fuel. Then, $Ri \times TWE$ can be calculated as the mole fraction of vaporized fuel is determined by the partial pressure of fuel molecule. Table 5.1 summarizes the vapor pressure (P_{vap}) and $Ri \times TWE$ at P_{vap}. nC7 and iC8 exhibit the highest values of $Ri \times TWE$, while others have low values.

When liquid fuel droplets are sprayed in the system, the composition in the fuel droplet will change over the fuel evaporation process, thus causing the impact of preferential vaporization. In this study, the extent of fuel vaporization is too small due to the short residence time of fuel droplet near the flame. In this regard, initial composition of fuel droplet is changed to investigate the impact of preferential vaporization instead of controlling the extent of fuel vaporization.

Considering that 135 TMB and nC12 exhibit identical behavior of extinction strain rate of methane diffusion flame and $Ri \times TWE$ values of 135 TMB and nC12 are negligible compared to that of nC7, nC7/135 and nC7/nC12 mixtures were prepared at different mole fraction of nC7 in the mixtures to observe the impact of fuel volatility. Figure 5.4(a) shows the methane mole fraction at the flame extinction as a function of nC7 mole fraction for the mixtures at $a = 40\ s^{-1}$. Two mixtures exhibit identical

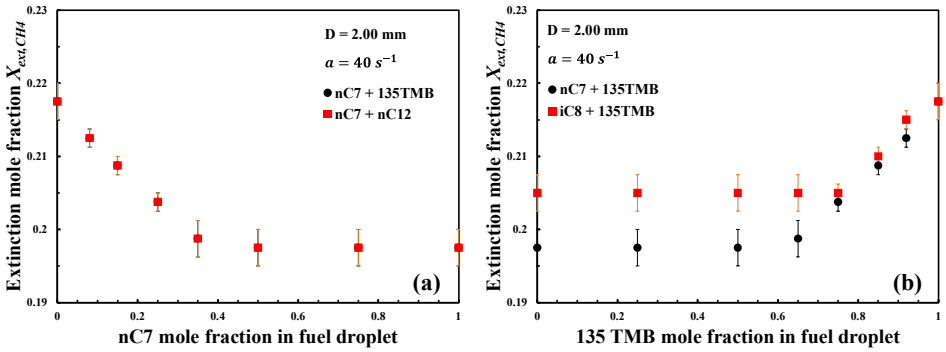

Figure 5.4. Extinction mole fraction of methane as a function of (a) nC7 mole fraction and (b) 135 TMB mole fraction in fuel droplet at $a = 40\ s^{-1}$ and D = 2.00 mm.

behavior, confirming that volatile component governs the extinction behavior when the components in liquid fuel have huge difference in the vapor pressure.

Furthermore, nC7/135 TMB and iC8/135TMB mixtures were formulated at different 135 TMB mole fractions to observe the impact of $Ri \times TWE$. Figure 5.4(b) shows the extinction mole fraction of methane at diffusion flame extinction as a function of 135 TMB mole fraction in fuel droplet at $a = 40\ s^{-1}$. The extinction mole fraction of methane is nearly constant until the 135 TMB mole fraction of 0.7. Then, it linearly increases, while the extinction mole fraction of methane for nC7/135 TMB mixture shows slightly higher value than that for iC8/135 TMB mixture. At given 135 TMB mole fraction, two mixtures have identical vaporization characteristic as the vapor pressures of nC7 and iC8 are similar at 300 K. Therefore, the difference in the extinction mole fraction of methane represents the impact of $Ri \times TWE$ from the mixtures having identical vaporization characteristic.

As previously mentioned, the composition in multi-component liquid fuel droplet changes over the fuel evaporation. Therefore, considering that the change in either nC7 or 135 TMB mole fraction in the mixtures shown Fig. 5.4(a) and (b) represents the variation of composition during the fuel evaporation, the decrease (increase) tendency in Fig. 5.4(a) (Fig. 5.4(b)) indicates that the preferential vaporization plays an important role in determining diffusion flame extinction by providing the enthalpy represented as $Ri \times TWE$.

5.3 Interaction between isolated single droplet and premixed flame

When the liquid fuel droplet is vaporized near the premixed flame, it provides the vaporized fuel to the flame, thus increasing local equivalence ratio. Heat release rate from

the premixed flame increases up to the stoichiometric condition, and then it decreases at higher equivalence ratio. Therefore, single droplet evaporating in the thermal diffusion layer of flame interacts with the premixed flame by changing local equivalence ratio. In this sense, the extinction of methane/air premixed flame with the fuel droplets was investigated to observe the interaction between single droplet and premixed flame.

Figure 5.5(a) shows the extinction strain rate of methane/air premixed flame as a function of equivalence ratio (φ) without the fuel droplet. The extinction strain rate exhibits the typical trend that has the maximum value at $\varphi = 1$ and $\varphi = 1.1$. In this study, the equivalence ratios in turbulent regime are not used to eliminate the impact of flow fluctuation generated by the turbulence. Among the lean and rich methane/air mixtures, the equivalence ratio of 1.5 is selected to investigate the impact of preferential vaporization as the fuel evaporation near the flame increases local equivalence ratio at fuel lean condition. It is noted that there was no difference in the extinction strain rate with fuel droplets for lean premixed flame in laminar regime due to additional fuel supply through the fuel vaporization. Even, high volatile fuels (e.g., nC7 and iC8) were not used as the methane premixed flame at the equivalence ratio of 1.5 is extinguished before the fuel droplets reach to the flame due to the prevaporized portion of liquid fuel droplet at

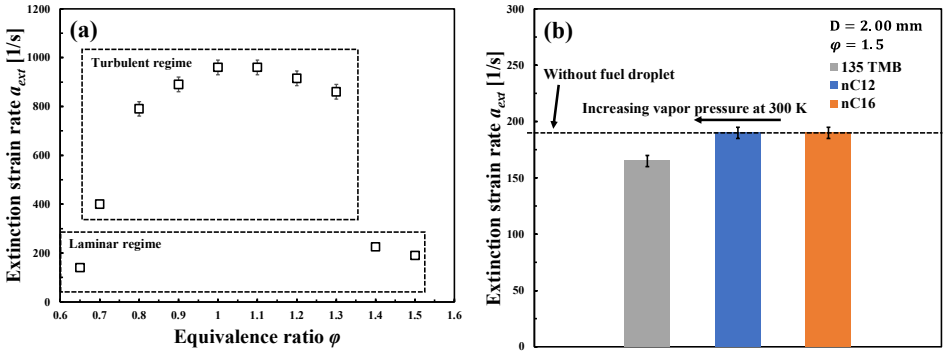

Figure 5.5. (a) Extinction stain rate of methane/air premixed flame as a function of equivalence ratio without fuel droplet and (b) comparison in extinction strain rate among 135 TMB, nC12, and nC16 at $\varphi = 1.5$ and D = 2.00 mm.

the upstream. Figure 5.5(b) shows the extinction strain rate of methane/air premixed flame at $\varphi = 1.5$ and $\mathrm{D} = 2.00$ mm for 135 TMB, nC12, and nC16. Compared to the extinction strain rate without fuel droplet, the extinction strain rates of nC12 and nC16 show no difference, while 135 TMB exhibits lower the extinction strain rate. Considering the partial pressure on the droplet surface, the extent of fuel vaporization of 135 TMB during short residence time is higher than that of nC12 and nC16, thus lower extinction strain rate for 135 TMB. This result implies that the fuel evaporation characteristic plays an important role in determining the extinction strain rate rather than the chemical kinetic impact.

CHAPTER 6

CONCLUSIONS

Energy conversion systems using combustion technologies such as gas turbines and aviation engines have not considered the chemical property change over the physical properties of liquid fuels. However, the needs to resolve the issues associated with fuel flexibility and pollutant emission arise other problems that the historical approaches to evaluate fuel properties for the engine operation should be modified. Specifically, the characteristics of fuel vaporization can cause unexpected combustion behaviors due to abrupt change in fuel composition that plays an important role in chemical kinetic characteristics. Therefore, to explore the impact of preferential vaporization, the flame flashback and flame extinction behaviors were investigated with liquid fuels. In chapter 2, the chemical reactivity potential represented as DCN was briefly discussed for Jet fuels, gasoline, and diesel.

In chapter 3, the impact of preferential vaporization on flame flashback behaviors was systematically investigated experimentally with a recently developed spray burner that can vary the fraction of fuel vaporized from a well-defined droplet spray. Spray characteristics at the nozzle exit of the spray burner were determined by using the PDPA technique. The results show that the spray burner is capable of controlling the extent of fuel vaporization by changing the flow residence time from atomization to the burner surface and the temperature of incoming air. Flame flashback behaviors were determined

at two conditions, fully- and partially vaporized conditions, by setting the burner and air flow temperature at 700 K and 450 K, respectively. The behaviors of four n-alkane fuels (nC7, nC8, nC12, and nC16) were compared against one another at fully vaporized conditions and results reveal a distinct flashback mechanism between propagation-driven and ignition-driven flashback mechanisms that depends on equivalence ratio.

To manifest the preferential vaporization impacts on flame flashback behaviors, two binary component fuel mixtures (nC8/iC16 and iC8/nC16 mixtures) were formulated to share the same chemical functional group distributions for $(CH_2)_n$ and CH_3. At fully vaporized condition, the two binary component mixtures were found to exhibit almost identical flame flashback characteristics in both propagation- and ignition-driven flashback regimes, confirming the methodology applied to formulate the fuel mixtures.

The impact of preferential vaporization on flame flashback was then investigated using the two binary component mixtures at partially vaporized conditions. Experiments were performed at two global equivalence ratios and different extents of fuel vaporization characterized by volume mean droplet diameter of fuel spray and its signal frequency measured utilizing PDPA. The measurements enabled the estimation of the effective equivalence ratio resulting from the local fuel vapor deposition.

The measured mean jet velocities at flashback for the two binary component mixtures were found to differ due to the difference in local laminar flame speeds caused by the preferential vaporization characteristics. Considering observed wrinkled flame structure at flashback and that the experimental conditions fall within the wrinkled flamelet regime of the Borghi diagram, the influence of local flow velocity perturbation due to instantaneous droplet vaporization was evaluated from PDPA velocity fluctuation

data. A pronounced increase in flashback velocity at leaner effective equivalence ratios was explained through differences in Markstein length and interpreting PLIF images.

Finally, the relative significance of local laminar flame speed, velocity perturbation, and preferential vaporization were determined through feature sensitivity analysis with a universal correlation that considers local laminar flame speed, local velocity fluctuation, and Markstein number. The results suggest that the local laminar flame speed and local velocity perturbation are of first-order significance in determining the flashback behaviors, while the impact of preferential vaporization is of second-order significance for the binary component fuel mixtures, nC8/iC16 and iCi/nC16 mixtures.

In chapter 4, the impact of preferential vaporization on the behavior of diffusion flame extinction was systematically investigated experimentally with a counterflow burner combined with the spray burner that can vary the fraction of fuel vaporized from a well-defined droplet spray. Extinction strain rate of spray diffusion flame was measured at $T_{Oxidizer} = 300\ K$ and $T_{Fuel} = 450\ K$. $Ri \times TWE$ of fully and partially vaporized fuels was used as an indicator to predict the extinction strain rate. The correlation equation between $Ri \times TWE$ and the extinction strain rate was found by measuring the extinction strain rate using single-component fuels at fully vaporized condition.

Based on $Ri \times TWE$, two different mixtures (nC8/iC16 and iC8/nC16) were formulated to have identical behavior of diffusion flame extinction at fully vaporized condition but have different vaporization characteristic. It was confirmed that the mixtures exhibit identical behavior of extinction strain rate.

The extinction strain rate was measured for the mixtures at different injector locations. The result cooperating with PDPA showed that the extinction strain rate of

Mixture 1 differs from that of Mixture 2 when the mixtures are partially vaporized. Even, the difference in the extinction strain rate became larger at lower extent of fuel evaporation.

The extinction strain rate of nC8 at fully vaporized condition exhibited that flow fluctuation at shorter injector location extinguishes the diffusion flame at lower strain rate. To account for the impact of flow fluctuation induced by spray dynamics and the phase change of liquid fuels, the extinction strain rate of nC8 was measured at near fully vaporized condition. Scaling parameter defined by the flow fluctuation and flame thickness to represent flow stretch induced by flow fluctuation was able to be correlated with the flow stretch.

The extinction strain rate including the flow stretch could be correlated with the radical index at partially vaporized condition and the transport weighted enthalpy based on OH PLIF images. The feature sensitivity analysis of the preferential vaporization and flow fluctuation on the extinction strain rate of diffusion flame revealed that the impact of preferential vaporization is relatively weaker than that of flow fluctuation. However, it is found that the preferential vaporization becomes effective to the extinction strain rate of diffusion flame when the mixtures are less vaporized.

In chapter 5, the interaction between isolated single droplet and flame was investigated by dripping the single droplets on methane/air diffusion and premixed flames. A droplet generator was developed to make single droplet using piezoelectric actuator operated by a function generator and amplifier. Measured velocity of fuel droplet is order of 1 m/s, resulting in the residence time of 1 ms near the flame. Therefore, the

vaporized composition can be determined by the initial mole fraction of liquid fuel due to shorter residence time of fuel droplet compared to the time for fuel evaporation.

The extinction strain rate of methane/air diffusion flame was measured at the droplet diameter of 0.46 and 2.00 mm. While the extinction strain rate did not change for the droplet size of 0.46 mm, it was found that the vapor pressure of fuel and the enthalpy including the chemical kinetic characteristic determines the extinction strain rate for the droplet size of 2.00 mm. Considering that the fuel mole fraction in the liquid droplet changes during the fuel evaporation, nC7/135 TMB, nC7/nC12, and iC8/135 TMB mixtures showed the influences of the vapor pressure and $Ri \times TWE$, thus the impact of preferential vaporization.

The interaction between fuel droplet and methane/air premixed was investigated at the equivalence ratio of 1.5. The result using 135 TMB, nC12, and nC16 suggested that the fuel evaporation characteristic plays an important role in determining the extinction strain rate rather than the chemical kinetic impact.

Through the discussions on the impact of preferential vaporization in this thesis, it is found that the variation of chemical kinetic characteristics of vaporized fuel over the evaporation of liquid fuel plays a considerable role in the combustion behaviors (e.g., flame flashback and flame extinction). In lab-scale experiment, it is not easy to observe the impact of preferential vaporization due to relatively small size of droplets in liquid fuel spray. Then, the preferential vaporization becomes more significant in determining the flame flashback behavior as large fuel droplets are able to penetrate the flame reaction zone, meaning that the effective equivalence ratio deviates further from the global equivalence ratio. In case of the diffusion flame extinction, large fuel droplets take longer

time to be fully vaporized. Then, not only effective fuel mole fraction but also interaction between fuel droplets and the flame will influence the extinction behavior through the preferential vaporization.

Compared to the experiment conducted in this thesis, the behavior of lean blowout (LBO) was investigated using a combustor test rig [13]. The LBO behavior was discussed based on the reactivity potential of distillation cuts due to the complexity of combustion behavior in the combustor test rig. It showed that the measured DCN of distillation cuts (20% liquid volume fraction each) can substantially change along with the distilled volume due to the characteristic of fuel evaporation. LBO behavior is dominated by fuel physical properties coupled with fuel chemical properties through the preferential vaporization at low temperature condition, while the chemical properties of entire fuel sample become a dominant factor on LBO behavior at increased temperature condition. In this regard, the experimental data and detailed analyses with lab-scale experimental apparatus in this thesis fundamentally support the LBO behavior.

REFERENCES

[1] F.L. Dryer, Chemical kinetic and combustion characteristics of transportation fuels, Proceedings of the Combustion Institute 35 (2015) 117-144.

[2] M. Stöhr, I. Boxx, C. Carter, W. Meier, Dynamics of lean blowout of a swirl-stabilized flame in a gas turbine model combustor, Proceedings of the Combustion Institute 33 (2011) 2953-2960.

[3] A. Ateshkadi, V.G. McDonell, G.S. Samuelsen, Lean blowout model for a spray-fired swirl-stabilized combustor, Proceedings of the Combustion Institute 28 (2000) 1281-1288.

[4] S.J. Shanbhogue, S. Husain, T. Lieuwen, Lean blowoff of bluff body stabilized flames: Scaling and dynamics, Progress in Energy and Combustion Science 35 (2009) 98-120.

[5] T.C. Lieuwen, Unsteady Combustor Physics, Cambridge University Press, Cambridge, 2012.

[6] W.-W. Kim, J.J. Lienau, P.R. Van Slooten, M.B. Colket, III, R.E. Malecki, S. Syed, Towards Modeling Lean Blow Out in Gas Turbine Flameholder Applications, Journal of Engineering for Gas Turbines and Power 128 (2004) 40-48.

[7] M. Colket, J. Heyne, M. Rumizen, M. Gupta, T. Edwards, W.M. Roquemore, G. Andac, R. Boehm, J. Lovett, R. Williams, J. Condevaux, D. Turner, N. Rizk, J. Tishkoff, C. Li, J. Moder, D. Friend, V. Sankaran, Overview of the National Jet Fuels Combustion Program, AIAA Journal 55 (2017) 1087-1104.

[8] L. Esclapez, P.C. Ma, E. Mayhew, R. Xu, S. Stouffer, T. Lee, H. Wang, M. Ihme, Fuel effects on lean blow-out in a realistic gas turbine combustor, Combustion and Flame 181 (2017) 82-99.

[9] A.H. Lefebvre, Fuel effects on gas turbine combustion-liner temperature, pattern factor, and pollutant emissions, Journal of Aircraft 21 (1984) 887-898.

[10] A.H. Lefebvre, Fuel Effects on Gas Turbine Combustion—Ignition, Stability, and Combustion Efficiency, Journal of Engineering for Gas Turbines and Power 107 (1985) 24-37.

[11] A.C.D.o.P. Products, Lubricants, Standard specification for aviation turbine fuel containing synthesized hydrocarbons, ASTM International2014.

[12] S.H. Won, P.S. Veloo, S. Dooley, J. Santner, F.M. Haas, Y. Ju, F.L. Dryer, Predicting the global combustion behaviors of petroleum-derived and alternative jet fuels by simple fuel property measurements, Fuel 168 (2016) 34-46.

[13] S.H. Won, N. Rock, S.J. Lim, S. Nates, D. Carpenter, B. Emerson, T. Lieuwen, T. Edwards, F.L. Dryer, Preferential vaporization impacts on lean blow-out of liquid fueled combustors, Combustion and Flame 205 (2019) 295-304.

[14] N. Rock, I. Chterev, B. Emerson, S.H. Won, J. Seitzman, T. Lieuwen, Liquid Fuel Property Effects on Lean Blowout in an Aircraft Relevant Combustor, Journal of Engineering for Gas Turbines and Power 141 (2019).

[15] S. Stouffer, T. Hendershott, J.R. Monfort, J. Diemer, E. Corporan, P. Wrzesinski, A.W. Caswell, Lean Blowout and Ignition Characteristics of Conventional and Surrogate Fuels Measured in a Swirl Stabilized Combustor, 55th AIAA Aerospace Sciences Meeting, American Institute of Aeronautics and Astronautics2017.

[16] N. Rock, B. Emerson, J. Seitzman, T. Lieuwen, Near-lean blowoff dynamics in a liquid fueled combustor, Combustion and Flame 212 (2020) 53-66.

[17] J.G. Colborn, J.S. Heyne, S.D. Stouffer, T.H. Hendershott, E. Corporan, Chemical and physical effects on lean blowout in a swirl-stabilized single-cup combustor, Proceedings of the Combustion Institute 38 (2021) 6309-6316.

[18] S.H. Won, F.M. Haas, S. Dooley, T. Edwards, F.L. Dryer, Reconstruction of chemical structure of real fuel by surrogate formulation based upon combustion property targets, Combustion and Flame 183 (2017) 39-49.

[19] V.R. Hasti, P. Kundu, G. Kumar, S.A. Drennan, S. Som, S.H. Won, F.L. Dryer, J.P. Gore, Lean blow-out (LBO) computations in a gas turbine combustor, 2018 Joint Propulsion Conference, American Institute of Aeronautics and Astronautics2018.

[20] N. Rock, I. Chterev, T. Smith, H. Ek, B. Emerson, D. Noble, J. Seitzman, T. Lieuwen, Reacting Pressurized Spray Combustor Dynamics: Part 1 — Fuel Sensitivities and Blowoff Characterization, 2016.

[21] N. Rock, I. Chterev, B. Emerson, J. Seitzman, T. Lieuwen, Blowout Sensitivities in a Liquid Fueled Combustor: Fuel Composition and Preheat Temperature Effects, 2017.

[22] S. Dooley, S.H. Won, F.M. Haas, J.S. Santner, Y. Ju, F.L. Dryer, T. Farouk, Development of Reduced Kinetic Models for Petroleum-Derived and Alternative Jet Fuels, 50th AIAA/ASME/SAE/ASEE Joint Propulsion Conference, American Institute of Aeronautics and Astronautics2014.

[23] C.K. Westbrook, W.J. Pitz, O. Herbinet, H.J. Curran, E.J. Silke, A comprehensive detailed chemical kinetic reaction mechanism for combustion of n-alkane hydrocarbons from n-octane to n-hexadecane, Combustion and Flame 156 (2009) 181-199.

[24] A. Bokhart, D. Shin, N.S. Rodrigues, P. Sojka, J.P. Gore, R.P. Lucht, Spray Characteristics of a Hybrid Airblast Pressure-Swirl Atomizer at Near Lean Blowout Conditions using Phase Doppler Anemometry, 2018 AIAA Aerospace Sciences Meeting, American Institute of Aeronautics and Astronautics2018.

[25] A. Stagni, L. Esclapez, P. Govindaraju, A. Cuoci, T. Faravelli, M. Ihme, The role of preferential evaporation on the ignition of multicomponent fuels in a homogeneous spray/air mixture, Proceedings of the Combustion Institute 36 (2017) 2483-2491.

[26] T. Edwards, L.Q. Maurice, Surrogate Mixtures to Represent Complex Aviation and Rocket Fuels, Journal of Propulsion and Power 17 (2001) 461-466.

[27] S. Dooley, S.H. Won, M. Chaos, J. Heyne, Y. Ju, F.L. Dryer, K. Kumar, C.-J. Sung, H. Wang, M.A. Oehlschlaeger, R.J. Santoro, T.A. Litzinger, A jet fuel surrogate formulated by real fuel properties, Combustion and Flame 157 (2010) 2333-2339.

[28] S. Dooley, S.H. Won, J. Heyne, T.I. Farouk, Y. Ju, F.L. Dryer, K. Kumar, X. Hui, C.-J. Sung, H. Wang, M.A. Oehlschlaeger, V. Iyer, S. Iyer, T.A. Litzinger, R.J. Santoro, T. Malewicki, K. Brezinsky, The experimental evaluation of a methodology for surrogate fuel formulation to emulate gas phase combustion kinetic phenomena, Combustion and Flame 159 (2012) 1444-1466.

[29] S. Dooley, S.H. Won, S. Jahangirian, Y. Ju, F.L. Dryer, H. Wang, M.A. Oehlschlaeger, The combustion kinetics of a synthetic paraffinic jet aviation fuel and a fundamentally formulated, experimentally validated surrogate fuel, Combustion and Flame 159 (2012) 3014-3020.

[30] F.L. Dryer, S. Jahangirian, S. Dooley, S.H. Won, J. Heyne, V.R. Iyer, T.A. Litzinger, R.J. Santoro, Emulating the Combustion Behavior of Real Jet Aviation Fuels by Surrogate Mixtures of Hydrocarbon Fluid Blends: Implications for Science and Engineering, Energy & Fuels 28 (2014) 3474-3485.

[31] S. Dooley, J. Heyne, S.H. Won, P. Dievart, Y. Ju, F.L. Dryer, Importance of a Cycloalkane Functionality in the Oxidation of a Real Fuel, Energy & Fuels 28 (2014) 7649-7661.

[32] H.J. Curran, P. Gaffuri, W.J. Pitz, C.K. Westbrook, A Comprehensive Modeling Study of n-Heptane Oxidation, Combustion and Flame 114 (1998) 149-177.

[33] A. Sudholt, L. Cai, J. Heyne, F.M. Haas, H. Pitsch, F.L. Dryer, Ignition characteristics of a bio-derived class of saturated and unsaturated furans for engine applications, Proceedings of the Combustion Institute 35 (2015) 2957-2965.

[34] F.M. Haas, A. Ramcharan, F.L. Dryer, Relative Reactivities of the Isomeric Butanols and Ethanol in an Ignition Quality Tester, Energy & Fuels 25 (2011) 3909-3916.

[35] M.E. Baumgardner, S.M. Sarathy, A.J. Marchese, Autoignition Characterization of Primary Reference Fuels and n-Heptane/n-Butanol Mixtures in a Constant Volume Combustion Device and Homogeneous Charge Compression Ignition Engine, Energy & Fuels 27 (2013) 7778-7789.

[36] ASTM D6890, doi:10.1520/d6890-18.

[37] ASTM D86, doi:10.1520/d0086-15.

[38] S. Japanwala, K.H. Chung, H.D. Dettman, M.R. Gray, Quality of Distillates from Repeated Recycle of Residue, Energy & Fuels 16 (2002) 477-484.

[39] J.L. Burger, J.A. Widegren, T.M. Lovestead, T.J. Bruno, 1H and 13C NMR Analysis of Gas Turbine Fuels As Applied to the Advanced Distillation Curve Method, Energy & Fuels 29 (2015) 4874-4885.

[40] A.G. Abdul Jameel, N. Naser, A.-H. Emwas, S. Dooley, S.M. Sarathy, Predicting Fuel Ignition Quality Using 1H NMR Spectroscopy and Multiple Linear Regression, Energy & Fuels 30 (2016) 9819-9835.

[41] B. Basu, G.S. Kapur, A.S. Sarpal, R. Meusinger, A Neural Network Approach to the Prediction of Cetane Number of Diesel Fuels Using Nuclear Magnetic Resonance (NMR) Spectroscopy, Energy & Fuels 17 (2003) 1570-1575.

[42] T. Lieuwen, V. McDonell, E. Petersen, D. Santavicca, Fuel Flexibility Influences on Premixed Combustor Blowout, Flashback, Autoignition, and Stability, Journal of Engineering for Gas Turbines and Power 130 (2008).

[43] B. Lewis, G. von Elbe, Stability and Structure of Burner Flames, The Journal of Chemical Physics 11 (1943) 75-97.

[44] G. von Elbe, M. Mentser, Further Studies of the Structure and Stability of Burner Flames, The Journal of Chemical Physics 13 (1945) 89-100.

[45] S.L. Plee, A.M. Mellor, Review of flashback reported in prevaporizing/premixing combustors, Combustion and Flame 32 (1978) 193-203.

[46] Y. Sommerer, D. Galley, T. Poinsot, S. Ducruix, F. Lacas, D. Veynante, Large eddy simulation and experimental study of flashback and blow-off in a lean partially premixed swirled burner, Journal of Turbulence 5 (2004).

[47] S.K. Dhanuka, J.E. Temme, J.F. Driscoll, H.C. Mongia, Vortex-shedding and mixing layer effects on periodic flashback in a lean premixed prevaporized gas turbine combustor, Proceedings of the Combustion Institute 32 (2009) 2901-2908.

[48] B. Shaffer, Z. Duan, V. McDonell, Study of Fuel Composition Effects on Flashback Using a Confined Jet Flame Burner, Journal of Engineering for Gas Turbines and Power 135 (2012).

[49] J. Kariuki, E. Mastorakos, Experimental investigation of turbulent flames in uniform dispersions of ethanol droplets, Combustion and Flame 179 (2017) 95-116.

[50] P.M. de Oliveira, P.M. Allison, E. Mastorakos, Ignition of uniform droplet-laden weakly turbulent flows following a laser spark, Combustion and Flame 199 (2019) 387-400.

[51] M. Mikami, S. Miyamoto, N. Kojima, Counterflow diffusion flame with polydisperse sprays, Proceedings of the Combustion Institute 29 (2002) 593-599.

[52] J.T. Zung, Evaporation Rate and Lifetimes of Clouds and Sprays in Air—The Cellular Model, The Journal of Chemical Physics 46 (1967) 2064-2070.

[53] J.M. Tishkoff, A model for the effect of droplet interactions on vaporization, International Journal of Heat and Mass Transfer 22 (1979) 1407-1415.

[54] S.H. Won, F.M. Haas, A. Tekawade, G. Kosiba, M.A. Oehlschlaeger, S. Dooley, F.L. Dryer, Combustion characteristics of C4 iso-alkane oligomers: Experimental characterization of iso-dodecane as a jet fuel surrogate component, Combustion and Flame 165 (2016) 137-143.

[55] S.H. Won, S. Dooley, P.S. Veloo, H. Wang, M.A. Oehlschlaeger, F.L. Dryer, Y. Ju, The combustion properties of 2,6,10-trimethyl dodecane and a chemical functional group analysis, Combustion and Flame 161 (2014) 826-834.

[56] D. Carpenter, S. Nates, F.L. Dryer, S.H. Won, Evaluating ignition propensity of high cycloparaffinic content alternative jet fuel by a chemical functional group approach, Combustion and Flame 223 (2021) 243-253.

[57] K. Dussan, S.H. Won, A.D. Ure, F.L. Dryer, S. Dooley, Chemical functional group descriptor for ignition propensity of large hydrocarbon liquid fuels, Proceedings of the Combustion Institute 37 (2019) 5083-5093.

[58] D. Kim, J. Martz, A. Violi, A surrogate for emulating the physical and chemical properties of conventional jet fuel, Combustion and Flame 161 (2014) 1489-1498.

[59] S.T. Lee, J.S. T'Ien, A numerical analysis of flame flashback in a premixed laminar system, Combustion and Flame 48 (1982) 273-285.

[60] V. Kurdyumov, E. Fernández-Tarrazo, J.M. Truffaut, J. Quinard, A. Wangher, G. Searby, Experimental and numerical study of premixed flame flashback, Proceedings of the Combustion Institute 31 (2007) 1275-1282.

[61] S.H. Won, B. Windom, B. Jiang, Y. Ju, The role of low temperature fuel chemistry on turbulent flame propagation, Combustion and Flame 161 (2014) 475-483.

[62] B. Windom, S.H. Won, C.B. Reuter, B. Jiang, Y. Ju, S. Hammack, T. Ombrello, C. Carter, Study of ignition chemistry on turbulent premixed flames of n-heptane/air by using a reactor assisted turbulent slot burner, Combustion and Flame 169 (2016) 19-29.

[63] J. Yanowitz, M.A. Ratcliff, R.L. McCormick, J.D. Taylor, M.J. Murphy, Compendium of Experimental Cetane Numbers, United States, 2017-02-22, 2017.

[64] S.M. Sarathy, C.K. Westbrook, M. Mehl, W.J. Pitz, C. Togbe, P. Dagaut, H. Wang, M.A. Oehlschlaeger, U. Niemann, K. Seshadri, P.S. Veloo, C. Ji, F.N. Egolfopoulos, T. Lu, Comprehensive chemical kinetic modeling of the oxidation of 2-methylalkanes from C7 to C20, Combustion and Flame 158 (2011) 2338-2357.

[65] E. Ranzi, A Wide-Range Kinetic Modeling Study of Oxidation and Combustion of Transportation Fuels and Surrogate Mixtures, Energy & Fuels 20 (2006) 1024-1032.

[66] H.-P.S. Shen, J. Steinberg, J. Vanderover, M.A. Oehlschlaeger, A Shock Tube Study of the Ignition of n-Heptane, n-Decane, n-Dodecane, and n-Tetradecane at Elevated Pressures, Energy & Fuels 23 (2009) 2482-2489.

[67] K. Zhang, C. Banyon, U. Burke, G. Kukkadapu, S.W. Wagnon, M. Mehl, H.J. Curran, C.K. Westbrook, W.J. Pitz, An experimental and kinetic modeling study of the oxidation of hexane isomers: Developing consistent reaction rate rules for alkanes, Combustion and Flame 206 (2019) 123-137.

[68] C. Ji, S.M. Sarathy, P.S. Veloo, C.K. Westbrook, F.N. Egolfopoulos, Effects of fuel branching on the propagation of octane isomers flames, Combustion and Flame 159 (2012) 1426-1436.

[69] C.K. Westbrook, W.J. Pitz, H.C. Curran, J. Boercker, E. Kunrath, Chemical kinetic modeling study of shock tube ignition of heptane isomers, International Journal of Chemical Kinetics 33 (2001) 868-877.

[70] B. Abramzon, W.A. Sirignano, Droplet vaporization model for spray combustion calculations, International Journal of Heat and Mass Transfer 32 (1989) 1605-1618.

[71] W.A. Sirignano, Fuel droplet vaporization and spray combustion theory, Progress in Energy and Combustion Science 9 (1983) 291-322.

[72] J.H. Burgoyne, L. Cohen, D.M. Newitt, The effect of drop size on flame propagation in liquid aerosols, Proceedings of the Royal Society of London. Series A. Mathematical and Physical Sciences 225 (1954) 375-392.

[73] Y. Nunome, S. Kato, K. Maruta, H. Kobayashi, T. Niioka, Flame propagation of n-decane spray in microgravity, Proceedings of the Combustion Institute 29 (2002) 2621-2626.

[74] S. Hayashi, T. Ohtani, K. Iinuma, S. Kumagai, Limiting factor of flame propagation in low-volatility fuel clouds, Symposium (International) on Combustion 18 (1981) 361-367.

[75] D. Bradley, M. Lawes, S. Liao, A. Saat, Laminar mass burning and entrainment velocities and flame instabilities of i-octane, ethanol and hydrous ethanol/air aerosols, Combustion and Flame 161 (2014) 1620-1632.

[76] R. Thimothée, C. Chauveau, F. Halter, I. Gökalp, Experimental Investigation of the Mechanisms of Cellular Instabilities Developing on Spherical Two-Phase Flames, Combustion Science and Technology 188 (2016) 2026-2043.

[77] R. Thimothée, C. Chauveau, F. Halter, I. Gökalp, Experimental investigation of the passage of fuel droplets through a spherical two-phase flame, Proceedings of the Combustion Institute 36 (2017) 2549-2557.

[78] S. Kadowaki, T. Hasegawa, Numerical simulation of dynamics of premixed flames: flame instability and vortex–flame interaction, Progress in Energy and Combustion Science 31 (2005) 193-241.

[79] N. Peters, The turbulent burning velocity for large-scale and small-scale turbulence, Journal of Fluid Mechanics 384 (1999) 107-132.

[80] R. Borghi, On the Structure and Morphology of Turbulent Premixed Flames, in: C. Casci, C. Bruno (Eds.), Recent Advances in the Aerospace Sciences: In Honor of Luigi Crocco on His Seventy-fifth Birthday, Springer US, Boston, MA, 1985, pp. 117-138.

[81] M.Z. Haq, C.G.W. Sheppard, R. Woolley, D.A. Greenhalgh, R.D. Lockett, Wrinkling and curvature of laminar and turbulent premixed flames, Combustion and Flame 131 (2002) 1-15.

[82] J.F. Driscoll, Turbulent premixed combustion: Flamelet structure and its effect on turbulent burning velocities, Progress in Energy and Combustion Science 34 (2008) 91-134.

[83] C.J. Sun, C.J. Sung, L. He, C.K. Law, Dynamics of weakly stretched flames: quantitative description and extraction of global flame parameters, Combustion and Flame 118 (1999) 108-128.

[84] J.K. Bechtold, M. Matalon, The dependence of the Markstein length on stoichiometry, Combustion and Flame 127 (2001) 1906-1913.

[85] R. Addabbo, J.K. Bechtold, M. Matalon, Wrinkling of spherically expanding flames, Proceedings of the Combustion Institute 29 (2002) 1527-1535.

[86] J. Goldmeer, R. Symonds, P. Glaser, B. Mohammad, Z. Nagel, P. Perez-Diaz, Evaluation of Arabian Super Light Crude Oil for Use in a F-Class DLN Combustion System, 2014.

[87] K. Tada, K. Inoue, T. Kawakami, K. Saitoh, S. Tanimura, Expanding Fuel Flexibility in MHPS' Dry Low NOx Combustor, 2018.

[88] S.C. Gülen, Gas turbines for electric power generation, Cambridge University Press2019.

[89] S.H. Won, S.J. Lim, S. Nates, A.K. Alwahaibi, F.L. Dryer, F. Farid, M. Hase, Combustion characteristics of crude oils for gas turbine applications by DCN measurements and NMR spectroscopy, Proceedings of the Combustion Institute 38 (2021) 5463-5473.

[90] R.-H. Chen, M. Chaos, A. Kothawala, Lewis number effects in laminar diffusion flames near and away from extinction, Proceedings of the Combustion Institute 31 (2007) 1231-1237.

[91] F.F. Fachini, LARGE-ACTIVATION-ENERGY ASYMPTOTIC ANALYSIS OF MULTICOMPONENT-FUEL DIFFUSION FLAMES, Combustion Science and Technology 177 (2005) 1793-1811.

[92] A. Hamins, H. Thridandam, K. Seshadri, Structure and extinction of a counterflow partially premixed, diffusion flame, Chemical Engineering Science 40 (1985) 2027-2038.

[93] A. Liñán, The asymptotic structure of counterflow diffusion flames for large activation energies, Acta Astronautica 1 (1974) 1007-1039.

[94] A. Liñán, D. Martínez-Ruiz, M. Vera, A.L. Sánchez, The large-activation-energy analysis of extinction of counterflow diffusion flames with non-unity Lewis numbers of the fuel, Combustion and Flame 175 (2017) 91-106.

[95] R.V. Ravikrishna, A.B. Sahu, Advances in understanding combustion phenomena using non-premixed and partially premixed counterflow flames: A review, International Journal of Spray and Combustion Dynamics 10 (2017) 38-71.

[96] H. Tsuji, Counterflow diffusion flames, Progress in Energy and Combustion Science 8 (1982) 93-119.

[97] F.A. Williams, A review of flame extinction, Fire Safety Journal 3 (1981) 163-175.

[98] S.H. Won, S. Dooley, F.L. Dryer, Y. Ju, A radical index for the determination of the chemical kinetic contribution to diffusion flame extinction of large hydrocarbon fuels, Combustion and Flame 159 (2012) 541-551.

[99] A. Kitajima, T. Ueda, A. Matsuo, M. Miomoto, Experimental investigation of the flame structure and extinction of turbulent counterflow non-premixed flames, Symposium (International) on Combustion 26 (1996) 137-143.

[100] R. Matsuo, H. Naito, A. Yoshida, Extinguishment of counterflow diffusion flame stabilized in turbulent airflow by polydisperse water mist, Proceedings of the Combustion Institute 37 (2019) 4239-4246.

[101] H. Tsuji, A. Yoshida, N. Endo, Effect of turbulence on extinction of counterflow diffusion flame, Symposium (International) on Combustion 25 (1994) 1191-1197.

[102] A. Kitajima, T. Ueda, A. Matsuo, M. Mizomoto, A comprehensive examination of the structure and extinction of turbulent nonpremixed flames formed in a counterflow, Combustion and Flame 121 (2000) 301-311.

[103] Y.-C. Chen, N. Peters, G.A. Schneemann, N. Wruck, U. Renz, M.S. Mansour, The detailed flame structure of highly stretched turbulent premixed methane-air flames, Combustion and Flame 107 (1996) 223-IN222.

[104] S.K. Choi, E.-S. Cho, S.H. Chung, Quantification of extinction mechanism in counterflow premixed flames, Journal of Mechanical Science and Technology 28 (2014) 3863-3871.

[105] G. Dixon-Lewis, Laminar premixed flame extinction limits. I. Combined effects of stretch and upstream heat loss in the twin-flame unburnt-to-unburnt opposed flow configuration, Proceedings of the Royal Society of London. Series A: Mathematical, Physical and Engineering Sciences 452 (1996) 1857-1884.

[106] A.M. Gamal, A.H. Ibrahim, E.-M.M. Ali, F.M. Elmahallawy, A. Abdelhafez, M.A. Nemitallah, S.S. Rashwan, M.A. Habib, Structure and Lean Extinction of Premixed Flames Stabilized on Conductive Perforated Plates, Energy & Fuels 31 (2017) 1980-1992.

[107] C.K. Law, Dynamics of stretched flames, Symposium (International) on Combustion 22 (1989) 1381-1402.

[108] J.i. Sato, Effects of lewis number on extinction behavior of premixed flames in a stagnation flow, Symposium (International) on Combustion 19 (1982) 1541-1548.

[109] S.H. Sohrab, C.K. Law, Extinction of premixed flames by stretch and radiative loss, International Journal of Heat and Mass Transfer 27 (1984) 291-300.

[110] N. Chigier, Group combustion models and laser diagnostic methods in sprays: A review, Combustion and Flame 51 (1983) 127-139.

[111] H. Kim, N. Sung, The effect of ambient pressure on the evaporation of a single droplet and a spray, Combustion and Flame 135 (2003) 261-270.

[112] T. Kitano, J. Nishio, R. Kurose, S. Komori, Evaporation and combustion of multicomponent fuel droplets, Fuel 136 (2014) 219-225.

[113] C.K. Law, S. Prakash, W.A. Sirignano, Theory of convective, transient, multicomponent droplet vaporization, Symposium (International) on Combustion 16 (1977) 605-617.

[114] J. Réveillon, L. Vervisch, Spray vaporization in nonpremixed turbulent combustion modeling: a single droplet model, Combustion and Flame 121 (2000) 75-90.

[115] T.I. Farouk, S.H. Won, F.L. Dryer, Sub-millimeter sized multi-component jet fuel surrogate droplet combustion: Physicochemical preferential vaporization effects, Proceedings of the Combustion Institute 38 (2021) 3313-3323.